Time Domain Modeling of Hybrid Electromagnetic and Thermal Processes

By

Wei Liu
B. Eng, University of Science and Technology of China, 1998

A Thesis Submitted in Partial Fulfillment of the
Requirements for the Degree of

MASTER OF APPLIED SCIENCE

In the Department of Electrical and Computer Engineering

We accept this thesis as conforming
To the required standard

[redacted]

Dr. W. J. R. Hoefer, Supervisor
Professor, Department of Electrical and Computer Engineering

[redacted]

Dr. Maria Stuchly, Department Member
Professor, Department of Electrical and Computer Engineering

[redacted]

Dr. James W. Provan, Outside Member
Professor, Department of Mechanical Engineering

[redacted]

Dr. Sadik Dost, External Examiner
Professor, Department of Mechanical Engineering

University of Victoria

Supervisor: Dr. Wolfgang J. R. Hoefer

ABSTRACT

The purpose of hybrid numerical analysis is to combine the advantages of different methods, and at the same time, avoid their disadvantages. In this thesis, two hybrid combinations of numerical methods that yield better numerical performance than any of the methods alone have been developed. The thesis comprises two distinct parts.

Part one describes the hybrid combination of the MRTD (wavelet based multiresolution time domain method) and the TLM method. A small section of part one is devoted to the technique of ATLM, which is useful in eliminating spurious solutions by eliminating computational redundancy.

Part two describes a new approach for modeling the thermal behavior of waveguide components under high-power operating conditions. Three mechanisms of heat transfer have been investigated, namely conduction, convection and radiation. This hybrid electromagnetic/thermal algorithm is very useful for microwave engineers in shortening the time for designing high-power waveguide components

Examiners:

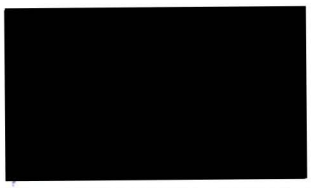

Dr. W. J. R. Hoefer, Supervisor
Professor, Department of Electrical and Computer Engineering

Dr. Maria Stuchly, Department Member
Professor, Department of Electrical and Computer Engineering

Dr. James W. Provan, Outside Member
Professor, Department of Mechanical Engineering

Dr. Sadik Dost, External Examiner
Professor, Department of Mechanical Engineering

Contents:

Abstract ii

Table of Contents iv

List of Figures vii

Acknowledgements ix

Dedication xi

List of Symbols xii

Chapter 1 Introduction 1

1.1 Background 1
1.1.1 Classification of Numerical Methods 1
1.1.2 Time Domain Numerical Methods 2
1.1.3 Advantages of Time Domain analysis 3
1.1.4 The TLM Method to solve the Electromagnetic Problem 4
1.2 Motivation 5
1.3 Original Contribution 6
1.4 Structure of the Thesis 7

Chapter 2 Hybrid Combination of TLM with MRTD 10

2.1 Introduction 10
2.2 Combination of TLM and MRTD Algorithms 11
2.2.1 Models for Haar Wavelet MRTD and 2D TLM Shunt Node 11
2.3 Connection Algorithm 15
2.4 PEC boundary conditions for MRTD 20
2.5 Numerical Validation 22

Chapter 3 Hybrid Combination of ATLM and MRTD 25

3.1 Introduction 25
3.2 Concepts of ATLM 26
3.3 Hybrid ATLM-MRTD Scheme 31
3.4 Numerical Validation 32

Chapter 4 Power Dissipation in Microwave Theory 36

4.1 Introduction 36
4.2 Perfect Conductor 36
4.3 Power Absorbed by Good Conductors and Dielectric Objects 37
4.3.1 Poynting's Theorem 37
4.3.2 Power Absorbed by a Good Conductor 39
4.3.3 Modeling of Lossy Conducting Walls in the TLM Method 42

4.4 Power Handling Capability 44
4.5 Conclusion 46

Chapter 5 Thermal Conduction 47

5.1 Introduction 47
5.2 Definition of Importance in General Heat Transfer 48
5.2.1 Specific Heat 48
5.3 Definition of Importance in Heat Conduction 48
5.3.1 Thermal Conductivity of Homogeneous Materials 48
5.3.2 Thermal diffusivity 50
5.4 Governing Law and Heat Conduction Equations 50
5.4.1 Fourier's law 50
5.4.2 General Heat Conduction Equation 51
5.5 Numerical Methods for Heat Conduction 52
5.5.1 Finite Difference Approximations 53
5.5.2 Numerical Methods for Modeling Transient Thermal Conduction 55
5.5.3 Stability Criteria 56
5.5.4 Alternating Numerical Approach for Heat Conduction 58
5.6 Conclusion 62

Chapter 6 Thermal Convection 63

6.1 Introduction 63
6.2 Definitions of Interest in Thermal Convection 63
6.2.1 The coefficient of thermal expansion 63
6.2.2 Dynamic Viscosity 64
6.2.3 Kinematic Viscosity 65
6.2.4 The Prandtl Number 66
6.3 Concept of Boundary Layer 66
6.4 Laminar and Turbulent Flow 67
6.5 Newton's law of cooling 69
6.6 Free convection 69
6.7 Evaluation of the heat transfer coefficient 71
6.8 Conclusion 76

Chapter 7 Thermal Radiation 77

7.1 Introduction 77
7.2 Definition of Interest in Thermal Radiation 78
7.2.1 Emissive power 78
7.2.2 Absorptivity, Reflectivity, and Transmissivity 79
7.3 Blackbody Radiation 80
7.3.1 The Stefan-Boltzman Law for Blackbody Emissive Power 80
7.4 Radiation of Nonblack Surfaces 81
7.4.1 Kirchhoff's Law 81
7.5 Shape Factor for Radiation Exchange 82
7.5.1 Calculation of Shape Factor 82
7.5.2 Properties of the Shape Factor 84
7.5.3 Shape Factor Between Two Arbitrary Sizes of Rectangular Planes 86

7.6 Lumped Thermal Capacity Model for Combined Convection and Radiation 93
7.6.1 Governing Equation and Initial Condition 94
7.7 Conclusion 97

Chapter 8 Numerical Analysis and Simulation Results 98

8.1 Numerical Analysis 98
8.1.1 Comprehensive Formulation 98
8.1.2 Flow Chart 104
8.2 Simulations Results 105
8.3 Error Analysis 109

Chapter 9 Conclusion 110

9.1 Conclusion 110
9.2 Future Research 112

Bibliography 114

List of Figures:

Figure. 2.1 Basis functions of the 2D MRTD Haar wavelet scheme. ϕ is Haar scaling function, ψ is Haar wavelet function. The gray areas show where the value of the functions is 1, otherwise it is –1. 12

Figure. 2.2 2D TLM Shunt Node 13

Figure. 2.3 Interface between MRTD and TLM mesh 14

Figure. 2.4 Upper side PEC boundary, in z direction 20

Figure. 2.5 Sampled time domain response: stable for about 900 MRTD time steps 23

Figure. 2.6 Sampled time domain response: unstable after 900 MRTD time steps 23

Figure. 2.7 Fourier transform of sampled time domain signals 23

Figure. 3.1 Traditional TLM boundary setting and a single scattering process. If the boundary of a structure is replaced by the cell boundary of a neighboring node, the illustration still works, except that the reflected pulse includes the pulse incident from the other node. 27

Figure. 3.2 Illustration on the wave pulse propagation in ATLM scheme. 28

Figure. 3.3 Illustration of the wave pulse propagation in the ATLM scheme when one node is continuously excited 29

Figure. 3.4 Illustration of the wave pulse propagation in the ATLM scheme when two neighboring nodes are excited at the same time step 30

Figure. 3.5 Instability appears in the simulation result obtained with the ATLM-MRTD scheme 33

Figure. 4.1 A volume V, enclosed by the closed surface S, containing fields $\overline{E}$, $\overline{H}$, and current sources $\overline{J_s}$, $\overline{M_s}$. 38

Figure. 4.2 Illustration on the calculation of power dissipation in good conductor 40

Figure. 5.1 Discretization cell (i, j, k) and the position of the scalar function values T and the vectors j 58

Figure. 5.2 Geometrical properties for the calculation of the discretized field component j_x 59

Figure. 6.1 Illustration on the boundary layer concept: laminar and turbulent flow 68

Figure. 6.2 Temperature and velocity distributions near a heated vertical surface in free convection flow 70

Figure. 6.3 Heated plates facing down (left) and facing up (right) 75

Figure. 7.1 Shape factor between two arbitrarily shaped and located surfaces 84

Figure. 7.2 Two rectangles of different sizes and placed in an arbitrary position 89

Figure. 7.3 Top view of two rectangles of different sizes and placed in an arbitrary position 92

Figure. 7.4 3D illustration of the lengths and angles used in above equations 93

Figure. 7.5 Schematic of a body losing heat by convection and radiation for a lumped thermal capacity model 94

Figure. 8.1 Topology of the structure: a microwave cavity with a PVC sample placed inside 105

Figure. 8.2 TE_{110} mode power distribution in a PVC (ε_r=3.5, σ=2.e-6 S/m) loaded cavity. In the 3D color representation, red (center) and deep blue (background) colors are corresponding to 0.0156-W and 0-W, respectively. The 2D wire mesh representation gives the same information in another perspective. 106

Figure. 8.3 Temperature distribution in the PVC loaded cavity. (a) Red (center) and deep blue (background) color are corresponding to 299.3^oK and 293^oK, respectively. The temperature evolution in the PVC block and in the air are shown in (b) and (c). The total power dissipated in the PVC region is 2-W, which is equivalent to a 0.0345^oK/s heating rate. This value agrees well with the slope of the graph in Figure. 8.3 (b), which is 0.0325^oK/s. 108

Figure. 8.4 Initial temperature distribution inside the computational domain with the excitation of TE210 mode field distribution 108

Figure. 8.5 Initial temperature distribution inside the computational domain with the excitation of TE220 mode field distribution 109

Acknowledgments

My work on this thesis would not have been accomplished without the help of a lot of people. I would like to take this precious opportunity to thank all of them for their kindly supports during my stay in University of Victoria.

Professor Wolfgang J. R. Hoefer, my supervisor, accepted me as a Master student after I graduated from University of Science and Technology of China in 1998. Thereafter, he has been giving tremendous help to my study and life in Victoria. As his student, I really enjoyed Prof. Hoefer's informative and interesting lectures I ever attended. Prof. Hoefer is also a good supervisor. He has been helping me a lot to overcome the difficulties that I encountered in the research. Without his guide, it must be impossible for me to finish the thesis work.

The members of the supervisory committee, Prof. Maria Stuchly and Prof. James Provan did a through proof reading and provided many helpful comments. Thank them very much for their patience. Prof. Sadik Dost has kindly agreed to be my external examiner and given me a lot of advice after he reviewed my thesis. Thanks him very much.

I really enjoyed the time I spent in the Computational Electromagnetics Research Lab. I would like to first thank Dr. Poman So for his great help and cooperation when we were working together on the implementation of thermal engine. I would also thank Dr. Masafumi Fujii for his patience and kindness. He helped me a lot getting familiar with UNIX system at the time I just arrived Canada. Without his help, I could neither have been able to study and understand TLM algorithm in that short time. Dr. Enqiu Hu, is not only a good colleague of mine, he and his wife, Ping, have also made me feel the home-

like warmth ever since we get to know each other. I want to thank Mr. Joon Woon Park and Dr. Mohamed Bakr, for creating such a nice research group in the lab. Thank Ms. Astrid Wright, you are really a great secretary and lovely lady.

Thank you all very much!

Wei Liu,

Victoria, March 15, 2001

To My Dear Family

献给我最亲爱的爸爸，妈妈和姐姐

List of Symbols

Symbols:

Symbol	:	Description
α	:	thermal diffusivity in thermal conduction
α	:	thermal absorptivity in thermal radiation
β	:	the coefficient of thermal expansion
C_p	:	specific heat
Γ_i	:	impulse reflection coefficient
G_r	:	the Grashof number
g	:	gravity
Δl_{MRTD}	:	MRTD mesh discretization size
Δl_{TLM}	:	TLM mesh discretization size
Δt_{MRTD}	:	time discretization interval in MRTD mesh
Δt_{TLM}	:	time discretization interval in TLM mesh
$\Delta x, \Delta y, \Delta z$	:	spatial discretization intervals in the $x, y,$ and z directions, respectively
ε	:	permittivity of dielectric material
E	:	electric field
E_λ	:	the monochromatic emissive power
F_{i-j}	:	the shape factor of area A_i with respect to area A_j
Z_l	:	TLM link line impedance
η	:	wave impedance
H	:	magnetic field
h	:	heat transfer coefficient
i	:	branch current in TLM mesh (denotes index if appears in the subsript)
$\bar{j}$	:	heat flux density
k	:	thermal conductivity (denotes index if appears in the subsript)
λ	:	wavelength
λ_c	:	cutoff wavelength
l	:	characteristic length
μ	:	permeability of magnetic material in Part I of the thesis
μ	:	constant of proportionality in Part II of the thesis
m	:	mass
N_u	:	the Nusselt number

v	:	incident or reflected voltage in TLM mesh in Part I of the thesis
v	:	fluid velocity in Part II of the thesis
ν	:	kinematic viscosity
P_{av}	:	average power
$\mathrm{P_r}$	:	the Prandtl number
ρ	:	density of material, also thermal reflectivity in thermal radiation
$\mathrm{R_a}$	:	the Rayleigh number
R_s	:	surface resistivity
σ	:	electric conductivity
σ_{SB}	:	Stefan-Boltzman constant
$\overline{S}$	:	Poynting vector
T	:	absolute temperature
τ	:	shearing stress in thermal convection
τ	:	thermal transmittivity in thermal radiation
ϕ	:	scaling function
ψ	:	wavelet function
ω	:	angular frequency

Notations:

Notations	:	**Description**
${}^{\zeta\xi}_{\omega}F^{n}_{i,j,k}$	:	expansion coefficient for the F_ω field component ($F = E, H$ and $\omega = x, y, z$) with respect to the basis functions $\zeta, \xi = \phi, \psi$ at time step n and spatial node (i, j, k)
${}_{inc}v^{n}_{i}$	:	incident voltage at the branch with index i (i =1, 2, 3, 4) at time step n in TLM mesh
i^{n}_{ω}	:	current in the direction ω ($\omega = x, y, z$) at the branch at time step n in TLM mesh

Common Abbreviations:

Abbreviations	:	**Description**
2-D	:	two-dimensional

3-D	:	three-dimensional
ABC	:	absorbing boundary condition
ATLM	:	alternating transmission line matrix
TD	:	time domain
TE	:	transverse electric
TEM	:	transverse electromagnetic
TLM	:	transmission line matrix
TM	:	transverse magnetic
FD	:	frequency domain
FDTD	:	finite-difference time-domain
MRTD	:	Multiresolution time domain
PEC	:	perfect electric conductor
PMC	:	perfect magnetic conductor
PVC	:	polyvinyl chloride
PXN	:	the power flux in negative X direction
PXP	:	the power flux in positive X direction
PYN	:	the power flux in negative Y direction
PYP	:	the power flux in positive Y direction
PZN	:	the power flux in negative Z direction
PZP	:	the power flux in positive Z direction
SCN	:	symmetrical condensed node

Chapter 1 Introduction

1.1 Background

The numerical analysis of systems of differential and integral equations has become a major issue in science and engineering. Each numerical method has its unique advantages, however, the limitations are also unavoidable. The purpose of hybrid numerical analysis is to combine the advantages of different methods, and at the same time, avoid their disadvantages.

1.1.1 Classification of Numerical Methods

It is possible to analytically solve the electromagnetic fields inside waveguide components when the structure is not too complicated. But, because most structures used today are not amenable to closed-form analytical expressions, numerical methods are essential for these types of applications.

One criterion for classification is the nature of the operators in the equations. It may be a differential or an integral operator. Another possible criterion is the domain in which the

operator, the field, and the source functions are defined. If these are defined in time, then the method is described as a time-domain method (TD). Alternatively, the frequency domain may be chosen, leading to frequency-domain methods (FD).

Clearly, the TD formulation is suitable for studying transients and nonlinear phenomena, while the FD formulation is appropriate for studying the steady-state response to a sinusoidal excitation. Any information available in the TD can be converted into the FD, and vice-versa. However, although the two descriptions are formally equivalent, issues of efficiency normally dictate which approach is the most convenient for a particular problem.

1.1.2 Time Domain Numerical Methods

Time domain analysis was, at least in the first half of the twentieth century, mostly performed in high voltage engineering in order to deal with transients due to switching, loading changes, breakdown and lightning. Later, the development of digital techniques for communications, measurement and high-speed logic has stimulated greater interest in time domain analysis, both at the circuit and the field levels.

In order to reduce the computational complexity of a field problem it is both reasonable and desirable to reduce the number of independent variables by using Fourier transformation techniques. In this way, assuming sinusoidal time dependence can eliminate the time dimension. Furthermore, if a structure is uniform in one or even two space dimensions, the problem can be broken down into simpler steady-state periodic solutions.

Discrete time domain models of electromagnetic fields can be obtained by discretizing time domain differential or integral formulations.

1.1.3 Advantages of Time Domain analysis

The principal advantages of modeling electromagnetic fields in the time domain are the following:

I. Non-sinusoidal waveforms and transient phenomena can be studied directly.

II. Nonlinear and frequency dispersive behavior can be modeled more physically in the time domain than in the frequency domain where the representation of these properties is mostly phenomenological.

III. Properties over a wide frequency band can be obtained with a single impulsive analysis.

IV. The geometry and electromagnetic material properties of a structure can be varied during a simulation through modeling of moving boundaries and time varying constitutive parameters.

V. Direct numerical synthesis is possible through reversal of electromagnetic processes in time.

VI. The results obtained are easier to interpret because the time domain formulation applies directly in space and time, the natural dimensions in which dynamic physical events are experienced.

1.1.4 The TLM Method to solve the Electromagnetic Problem

Transmission line modeling (TLM) provides a conceptual model, which produces a time domain numerical technique for solving networks and fields. Electromagnetic fields are modeled by filling the field space with a network of transmission lines, which renders the problem discrete in space and time since pulses launched on the network scatter from point to point in space in a fixed time step. Electric and magnetic fields are made equivalent to voltages and currents on the network. The numerical calculation usually starts by exciting the network at specific points by voltage or current impulses and tracks the propagation of these impulses over the network as they are scattered by the nodes and branches at boundaries.

The main advantange of the TLM method is:

I. The ease with which even the most complicated structures can be analyzed.

II. As far as computational expenditure is concerned, TLM method compares favorably with finite-element and finite-difference methods.

III. The passive nature of the TLM network model and the use of scattering rather than finite differencing guaranties stability and numerical robustness.

IV. Another advantage resides in the large amount of information generated in one single computation. Not only is the impulse response of a structure obtained, yielding in turn, its response to any excitation, but also the characteristics of the dominant and higher order modes are accessible in the frequency domain through the Fourier transform

V. Since TLM operates in the time domain, it can directly account for time-dependant properties of structures, i.e., variations in material properties during the simulation.

1.2 Motivation

Any numerical method has its unique advantages as well as some unavoidable limitations. For example, although wavelet based time-domain techniques can reduce the computational effort and by virtue of thresholding techniques, may also save memory, it is very difficult to realize complicated boundary conditions when using wavelets. However, the TLM method is very powerful when applied to model with complicated boundary conditions. Speaking of the thermal application such as predicting the temperature rise and distribution in waveguide components or optimizing the power handling capability of high power waveguide components, the TLM method is not as straightforward to apply as FDTD. FDTD can approximate the equation governing thermal conduction without the need for an equivalent electrical network and is thus very popular in thermal applications.

The work in this thesis is originally motivated by the need to solve problems such as discussed above. A hybrid solution is sought that will be able to simultaneously take advantage of the strengths of several numerical methods while minimizing the effects of their shortcomings or even try to compensate. Several hybrid approaches have been derived, implemented and tested in this thesis, and the conclusions will be very useful for further research.

1.3 Original Contribution

The main contribution of this thesis is the development of two novel hybrid combinations of numerical methods that yield better numerical performance than any of the methods alone. The thesis thus comprises two distinct parts. Part one describes the hybrid combination of the MRTD (wavelet based multiresolution time domain method) and the TLM method. A small section of part one is devoted to the technique of ATLM, which is useful in eliminating spurious solutions by eliminating computational redundancy. Although the complex implementation of ATLM leads to a late-time instability of the hybrid scheme, this first attempt will serve as a useful starting point for further research on this topic.

Part two of the thesis describes a new approach for modeling the thermal behavior of waveguide components under high-power operating conditions. In addition to microwave heating, conventional heating can be modeled and simulated with the thermal part of the algorithm as well. Three mechanisms of heat transfer have been investigated.

First, the important material properties and concepts used in the thermal application are discussed in detail. The diffusion of heat through conduction is computed not only in homogeneous but also inhomogeneous bodies that have different zones with different thermal properties. Temperature dependence of thermal conductivity is also taken into account.

Thermal convection is modeled under the assumption that no cooling system is present so that only natural convection is simulated. Calculation of the Nusselt number to obtain the heat transfer coefficient is also discussed.

As to the process of thermal radiation, both free radiation and thermal heat exchange by radiation are modeled. Free radiation is rather straightforward to simulate, however, the analysis of thermal heat exchange between mutually visible surfaces can require tremendous effort. The hardest part is to determine the shape factors between the surfaces of arbitrary shape, at arbitrary location. Some empirical formulae are presented, but we will also point out some simplifying assumptions in the numerical calculation of the shape factors, such as the assumption that the cell surface is of infinitely small area so that it can be considered as a point object. However, this requires a small time step and may lead to a huge computation effort. Thus, one may want to opt for a tradeoff between these possibilities.

The simulation results show a temperature evolution curve that is physically meaningful, and the temperature distribution also corresponds to that of the source power distribution. However, due to the complexity of the thermal situation, it is hard to find reliable experimental data for validation. Thus, some approximate evaluation of the hybrid algorithm has been performed.

The hybrid electromagnetic/thermal algorithm is potentially very useful for microwave engineers in shortening the time for designing high-power waveguide components. It allows to predict the temperature rise, to identify potential hot spots, to predict the critical time constants and to optimize the power handling capability.

1.4 Structure of the Thesis

This thesis is organized into nine chapters. After the introduction, Chapter 2 and Chapter 3 form Part I of the thesis. Two hybrid combinations of numerical methods, namely

TLM-MRTD and ATLM-MRTD, form the subject of Part 1. Their derivation, implementation and testing are described

The subject of Part II is the hybrid combination of an electromagnetic TLM scheme with a thermal model including conduction, convection, and radiation of heat. . Chapter 4 first introduces the energy conservation equation according to Poynting's theory. Then the evaluation of power dissipated in good conductors and lossy dielectric materials is described. Power handling capability is defined and discussed in the last part of Chapter 4.

Chapters 5-7 are dedicated to three types of thermal processes: thermal conduction, thermal convection and thermal radiation. At the beginning of each of the three chapters, definitions pertaining to each specific heat transfer mode are presented. Then the governing equations are derived and modeled. Thermal conduction is formulated using an explicit FDTD scheme. Natural convection is taken relatively easily into account if certain assumptions and simplifications are made. Free thermal radiation is treated by means of empirical equations. The most difficult part is the calculation of shape factors, which is the subject of Chapter 7.

Chapter 8 first summarizes all the important formulas used in thermal part of the hybrid algorithm. Then simulation results are presented, followed by a discussion of the cause of errors.

Chapter 9 presents conclusion of the thesis work and discusses future research directions.

PART I

Coupled TLM-MRTD Analysis

Chapter 2 Hybrid Combination of TLM with MRTD

2.1 Introduction

Nowadays, wavelet based Multiresolution Time Domain Methods (MRTD) have become very popular in electromagnetic field modeling. One of the difficulties encountered when applying MRTD to realistic problems is the modeling of complex boundary conditions that can be more effectively handled with the traditional numerical time domain methods such as the TLM (Transmission Line Matrix) method. Hence, we have investigated a hybrid combination of MRTD and TLM such that the former is used to model subdomains of simple shape, while the latter models the complicated boundary geometry. Such a combination requires a technique for connecting MRTD and TLM along a common interface.

The objective of this chapter is to derive, implement and validate a MRTD/TLM connection algorithm. Although MRTD offers a potential reduction in computation time and memory due to a larger time step for equal space resolution compared with TLM, the advantage of the hybrid combination has not been fully demonstrated in this thesis by

applying it to a very large mesh. Rather, emphasis has been placed on the interface algorithm itself. We have used an MRTD scheme based on Haar wavelets, and the TLM 2D shunt node in this analysis. Both TLM and ATLM implementations have been derived and used in the combination algorithm.

2.2 Combination of TLM and MRTD Algorithms

2.2.1 Models for Haar Wavelet MRTD and 2D TLM Shunt Node

The hybrid algorithm is a combination of the 2D Haar wavelet MRTD and the 2D TLM shunt node.

The 2D basis functions used in the Haar wavelet MRTD and TLM shunt node are depicted in Figure. 2.1 and Figure. 2.2, respectively. Only basic information on the algorithms is provided here. Background theorem on wavelets in details can be found in the literature. For example, [1] Mallat, [2] Daubechies, [5]Rokhin-[7]Werthen and Wolff are some widely used references on this topic.

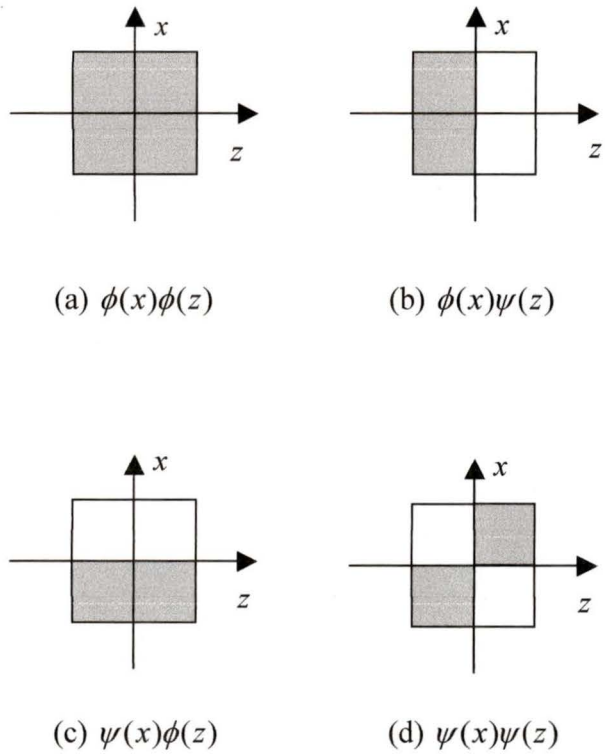

(a) $\phi(x)\phi(z)$ (b) $\phi(x)\psi(z)$

(c) $\psi(x)\phi(z)$ (d) $\psi(x)\psi(z)$

Figure. 2.1 Basis functions of the 2D MRTD Haar wavelet scheme. ϕ is Haar scaling function, ψ is Haar wavelet function. The gray areas show where the value of the functions is 1, otherwise it is –1.

The functions ϕ and ψ are defined as

$$\phi(s) = \begin{cases} 1 & \text{for} \quad |s| < 1/2 \\ 1/2 & \text{for} \quad |s| = 1/2 \\ 0 & \text{elsewhere} \end{cases} \tag{2.1}$$

$$\psi(s)=\begin{cases}1/2 & \text{for} \quad s=-1/2 \\ 1 & \text{for} \quad -1/2<s<0 \\ -1 & \text{for} \quad 0<s<1/2 \\ -1/2 & \text{for} \quad s=1/2 \\ 0 & \text{for} \quad s=0 \text{ and elsewhere}\end{cases} \tag{2.2}$$

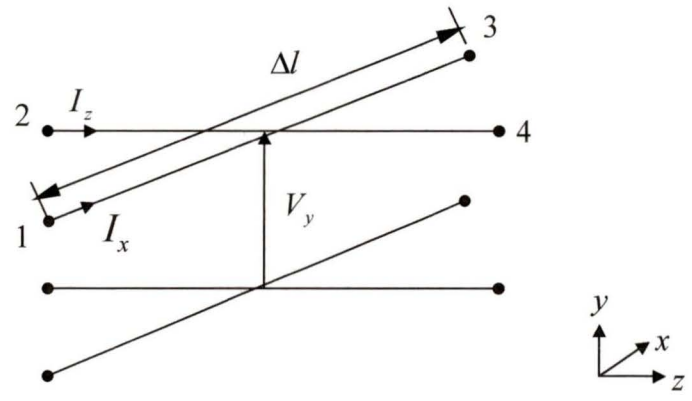

Figure. 2.2 2D TLM Shunt Node

The structure analyzed is an air filled square resonator. It was symmetrically divided into an MRTD and a TLM subdomain along the z direction. As shown in Figure. 2.3, the length of MRTD cell Δl_{MRTD} is twice that of TLM cell, Δl_{TLM} . The time step of MRTD is twice that of TLM as well. One MRTD cell and two TLM cells nodes are overlapped at the interface in such a way that the sampling points of the MRTD cell and the centers of the TLM cells are collocated which is illustrated in Figure. 2.3.

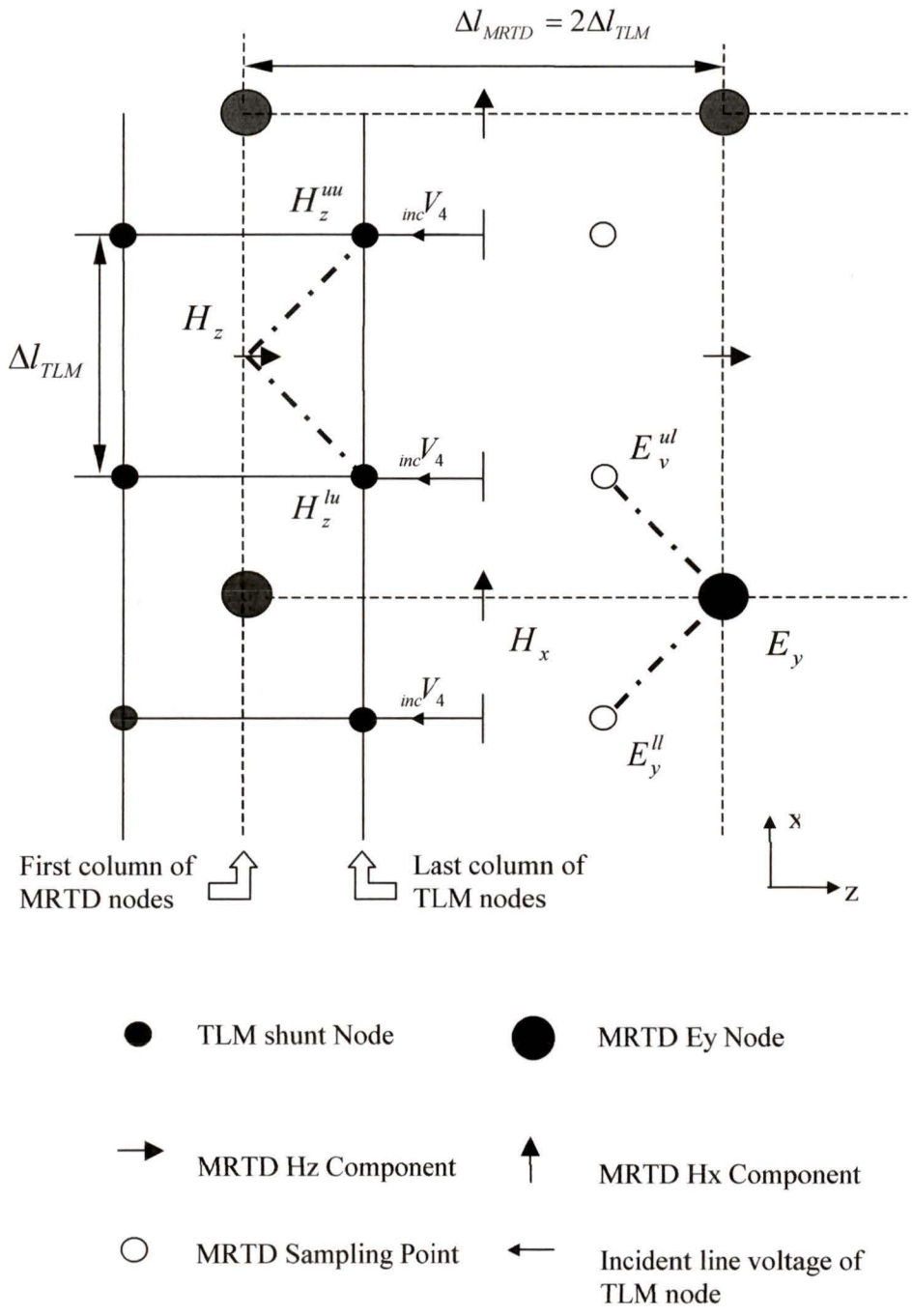

Figure. 2.3 Interface between MRTD and TLM mesh

2.3 Connection Algorithm

Consider the interface shown in Figure. 2.3, the steps of connection algorithm will be described below. In each iteration TLM scattering and connection processes take place twice while the updating of MRTD fields is performed only once. In the following derivation, "n" denotes the index of MRTD time step.

A. At Time Step " n "

The connection is first made between TLM node voltages and MRTD E-field. For data transfer from TLM to MRTD E-field, we first sample TLM node voltages at four TLM nodes that surround the MRTD E_y node as

$$\upsilon_y^n = \frac{1}{2}\left[{}_{inc}\upsilon_1^{n-1/4} + {}_{inc}\upsilon_2^{n-1/4} + {}_{inc}\upsilon_3^{n-1/4} + {}_{inc}\upsilon_4^{n-1/4} \right] \tag{2.3}$$

The relation between the TLM node voltage and MRTD E-field is defined by

$$E_y^n \equiv \upsilon_y^n \tag{2.4}$$

Then those four voltages are decomposed into the Haar wavelet basis by

$$\begin{bmatrix} {}^{\phi\phi}E_y^n \\ {}^{\phi\psi}E_y^n \\ {}^{\psi\phi}E_y^n \\ {}^{\psi\psi}E_y^n \end{bmatrix} = \frac{1}{4}\begin{bmatrix} 1 & 1 & 1 & 1 \\ 1 & -1 & 1 & -1 \\ 1 & 1 & -1 & -1 \\ 1 & -1 & -1 & 1 \end{bmatrix}\begin{bmatrix} {}^{ll}E_y^n \\ {}^{lu}E_y^n \\ {}^{ul}E_y^n \\ {}^{uu}E_y^n \end{bmatrix} \tag{2.5}$$

where ll, lu, ul and uu denote the corresponding Haar MRTD sampling points, for example, lu denotes the sampling point at the lower side in the x-direction and the upper side in the z-direction.

For data transfer from the MRTD E-field to TLM, the MRTD E-field at the TLM node centers on the last column of the TLM nodes are reconstructed by

$$\begin{bmatrix} {}^{ll}E_y^n \\ {}^{lu}E_y^n \\ {}^{ul}E_y^n \\ {}^{uu}E_y^n \end{bmatrix} = \begin{bmatrix} 1 & 1 & 1 & 1 \\ 1 & -1 & 1 & -1 \\ 1 & 1 & -1 & -1 \\ 1 & -1 & -1 & 1 \end{bmatrix} \begin{bmatrix} {}^{\phi\phi}E_y^n \\ {}^{\phi\psi}E_y^n \\ {}^{\psi\phi}E_y^n \\ {}^{\psi\psi}E_y^n \end{bmatrix} \tag{2.6}$$

Since these E-field values are equivalent to TLM node voltages as in (2.4), the incident pulse at the end of the TLM region can be estimated by

$$\begin{aligned} {}_{inc}\upsilon_4^{n-1/4} &= 2\upsilon_y^n - \left({}_{inc}\upsilon_1^{n-1/4} + {}_{inc}\upsilon_2^{n-1/4} + {}_{inc}\upsilon_3^{n-1/4} \right) \\ &= 2E_y^n - \left({}_{inc}\upsilon_1^{n-1/4} + {}_{inc}\upsilon_2^{n-1/4} + {}_{inc}\upsilon_3^{n-1/4} \right) \end{aligned} \tag{2.7}$$

Thus we have all the TLM incident pulses required for the following TLM scattering process.

B. Transition from "n" to "$n+1/2$"

The fields are now to be updated both in the TLM and Haar MRTD regions individually. For H-field update through Haar MRTD,

$${}_z^{\xi\eta}H_{i+1/2,k}^{n+1/4} = {}_z^{\xi\eta}H_{i+1/2,k}^{n-1/4} - \frac{\Delta t_M}{\mu \Delta l_M}\left({}_y^{\xi\eta}E_{i+1,k}^n - {}_y^{\xi\eta}E_{i,k}^n \right) \tag{2.8}$$

$$ {}^{\xi\eta}_{x}H^{n+1/4}_{i,k+1/2} = {}^{\xi\eta}_{x}H^{n-1/4}_{i,k+1/2} - \frac{\Delta t_M}{\mu \Delta l_M}\left({}^{\xi\eta}_{y}E^{n}_{i,k+1} - {}^{\xi\eta}_{y}E^{n}_{i,k} \right) \tag{2.9} $$

for $\xi, \eta = \phi, \psi$, where Δt_M and Δl_M denote the Haar MRTD time and space increments, i, k and n denote the index in the x, z directions and time, respectively.

For TLM, the standard 2D shunt node algorithm is performed, which consists of scattering and connection procedures

$$ {}_{ref}[V]^{n+1/4} = [S]\ {}_{inc}[V]^{n-1/4} \tag{2.10} $$

$$ {}_{inc}[V]^{n+1/4} = [C]\ {}_{ref}[V]^{n+1/4} \tag{2.11} $$

where $[S]$ is the scattering matrix and $[C]$ is the connection matrix. Note that for consistent excitation of TLM and MRTD regions, excitation is not occurred at this moment but occurred only at the following update step described later.

C. At. Time Step "$n + \frac{1}{2}$"

After updating H-field in MRTD, field data are transferred between TLM node currents and Haar MRTD H-field. For data transfer from the TLM node currents to the Haar MRTD H-fields, TLM node currents i_x are sampled at four TLM nodes that surround the MRTD H_z node as

$$ i_x^{n+1/2} = \frac{1}{Z_l}\left[{}_{inc}\upsilon_1^{n+1/4} - {}_{inc}\upsilon_3^{n+1/4} \right] \tag{2.12} $$

where Z_l is the TLM line-line impedance. Similarly, i_z are sampled at four TLM nodes that surround the MRTD H_x node as

$$i_z^{n+1/2} = \frac{1}{Z_l}\left[{}_{inc}\upsilon_2^{n+1/4} - {}_{inc}\upsilon_4^{n+1/4} \right] \tag{2.13}$$

Then these currents are converted to the MRTD H-field by

$$H_x^{n+1/2} \equiv -i_z^{n+1/2} \tag{2.14}$$

$$H_z^{n+1/2} \equiv i_x^{n+1/2} \tag{2.15}$$

Then the H-fields are decomposed into the Haar basis by

$$\begin{bmatrix} {}^{\phi\phi}H_w^{n+1/2} \\ {}^{\phi\psi}H_w^{n+1/2} \\ {}^{\psi\phi}H_w^{n+1/2} \\ {}^{\psi\psi}H_w^{n+1/2} \end{bmatrix} = \frac{1}{4}\begin{bmatrix} 1 & 1 & 1 & 1 \\ 1 & -1 & 1 & -1 \\ 1 & 1 & -1 & -1 \\ 1 & -1 & -1 & 1 \end{bmatrix}\begin{bmatrix} {}^{ll}H_w^{n+1/2} \\ {}^{lu}H_w^{n+1/2} \\ {}^{ul}H_w^{n+1/2} \\ {}^{uu}H_w^{n+1/2} \end{bmatrix} \tag{2.16}$$

for $w = x$ and y.

Inversely, data transfer from Haar MRTD H-fields to TLM node currents is achieved first by reconstructing H_x – fields

$$\begin{bmatrix} {}^{ll}H_x^{n+1/2} \\ {}^{lu}H_x^{n+1/2} \\ {}^{ul}H_x^{n+1/2} \\ {}^{uu}H_x^{n+1/2} \end{bmatrix} = \begin{bmatrix} 1 & 1 & 1 & 1 \\ 1 & -1 & 1 & -1 \\ 1 & 1 & -1 & -1 \\ 1 & -1 & -1 & 1 \end{bmatrix}\begin{bmatrix} {}^{\phi\phi}H_x^{n+1/2} \\ {}^{\phi\psi}H_x^{n+1/2} \\ {}^{\psi\phi}H_x^{n+1/2} \\ {}^{\psi\psi}H_x^{n+1/2} \end{bmatrix} \tag{2.17}$$

and then, with the relation (2.12), (2.13), (2.14) and (2.15), the incident pulses at the end of the TLM region can be estimated by

$$\begin{aligned} {}_{inc}\upsilon_4^{n+1/4} &= -Z_l i_z^{n+1/2} + {}_{inc}\upsilon_2^{n+1/4} \\ &= Z_l H_x^{n+1/2} + {}_{inc}\upsilon_2^{n+1/4} \end{aligned} \tag{2.18}$$

It is then possible to perform the next TLM scattering process.

D. Transition from "$n+\frac{1}{2}$" to "$n+1$"

The field values are now updated again with TLM and Haar MRTD R-update equation. The Haar MRTD E-update equation is given by

$$\begin{aligned} {}_y^{\xi\eta}E_{i,k}^{n+1} = {}_y^{\xi\eta}E_{i,k}^{n} + \\ \frac{\Delta t_M}{\varepsilon \Delta l_M}\left[{}_x^{\xi\eta}H_{i,k+1/2}^{n+1/2} - {}_x^{\xi\eta}H_{i,k-1/2}^{n+1/2} - \left({}_z^{\xi\eta}H_{i,k+1/2}^{n+1/2} - {}_z^{\xi\eta}H_{i,k-1/2}^{n+1/2} \right) \right] + {}_y^{\xi\eta}e_{i,k}^{n} \end{aligned} \tag{2.19}$$

for $\xi,\eta = \phi,\psi$, where ${}_y^{\xi\eta}e_{i,k}^{n}$ is the amplitude of an E-field excitation.

The same TLM algorithm as described above, together with an excitation process at this time, is executed as follows:

$${}_{ref}[V]^{n+1/4} = [S]_{inc}[V]^{n-1/4} + \frac{1}{2}e[I] \tag{2.20}$$

where [I] is the identity matrix. This excitation procedure gives smooth excitation distribution over the TLM and Haar regions. This concludes the connection algorithm, and the cycle is repeated.

2.4 PEC boundary conditions for MRTD

PEC boundary conditions for MRTD are derived in this section. For the convenience, boundary is set on E_y nodes in MRTD mesh. Upper side PEC boundary has been taken as an example for the derivation. As illustrated in Figure. 2.4, E_0 denotes the E_y node on the boundaries and E_1 denotes the E_y node immediately beside E_0. These denotations hold for the rest of this section.

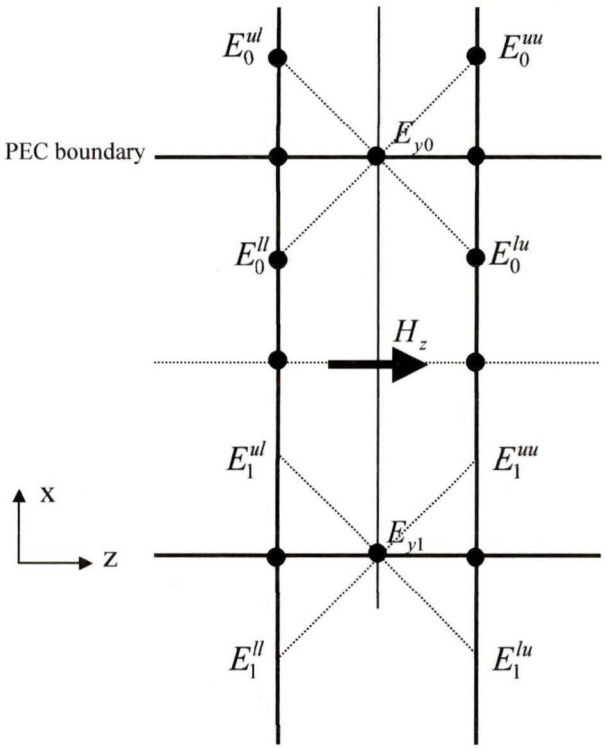

Figure. 2.4 Upper side PEC boundary, in z direction

The following equations are derived using the linear interpolation and the property that tangential electrical filed is zero on PEC boundary:

$$\begin{cases} E_0^{lu} = E_1^{uu}/3 & (a) \\ E_0^{ll} = E_1^{ul}/3 & (b) \\ E_0^{lu} + E_0^{uu} = 0 & (c) \\ E_0^{ll} + E_0^{ul} = 0 & (d) \end{cases} \tag{2.21}$$

Applying the equation (2.6) to (2.21), the coefficients of the field component are extracted:

$$\begin{aligned} &(a) \Rightarrow E_0^{\phi\phi} - E_0^{\phi\psi} + E_0^{\psi\phi} - E_0^{\psi\psi} = (E_1^{\phi\phi} - E_1^{\phi\psi} - E_1^{\psi\phi} + E_1^{\psi\psi})/3 \\ &(b) \Rightarrow E_0^{\phi\phi} + E_0^{\phi\psi} + E_0^{\psi\phi} + E_0^{\psi\psi} = (E_1^{\phi\phi} + E_1^{\phi\psi} - E_1^{\psi\phi} + E_1^{\psi\psi})/3 \\ &(c) \Rightarrow E_0^{\phi\phi} - E_0^{\phi\psi} = 0 \\ &(d) \Rightarrow E_0^{\phi\phi} + E_0^{\phi\psi} = 0 \end{aligned} \tag{2.22}$$

$$\Rightarrow \begin{cases} E_0^{\phi\phi} = 0 \\ E_0^{\phi\psi} = 0 \\ E_0^{\psi\phi} = (E_1^{\phi\phi} - E_1^{\psi\phi})/3 \\ E_0^{\psi\psi} = (E_1^{\phi\psi} - E_1^{\psi\psi})/3 \end{cases} \tag{2.23}$$

These are equations for updating E_y on upper side PEC boundaries. Similar reasoning gives the updating equations for E_y on lower side, right side, left side PEC boundaries in 2D case. The results are listed below:

$$Lower \quad PEC \quad \begin{cases} E_0^{\phi\phi} = 0 \\ E_0^{\phi\psi} = 0 \\ E_0^{\psi\phi} = -(E_1^{\phi\phi} + E_1^{\psi\phi})/3 \\ E_0^{\psi\psi} = -(E_1^{\phi\psi} + E_1^{\psi\psi})/3 \end{cases} \tag{2.24}$$

$$Right \quad PEC \qquad \begin{cases} E_0^{\phi\phi} = 0 \\ E_0^{\phi\psi} = (E_1^{\phi\phi} - E_1^{\phi\psi})/3 \\ E_0^{\psi\phi} = 0 \\ E_0^{\psi\psi} = (E_1^{\psi\phi} - E_1^{\psi\psi})/3 \end{cases} \tag{2.25}$$

$$Left \quad PEC \qquad \begin{cases} E_0^{\phi\phi} = 0 \\ E_0^{\phi\psi} = -(E_1^{\phi\phi} + E_1^{\phi\psi})/3 \\ E_0^{\psi\phi} = 0 \\ E_0^{\psi\psi} = -(E_1^{\psi\phi} + E_1^{\psi\psi})/3 \end{cases} \tag{2.26}$$

2.5 Numerical Validation

The algorithm has been applied to analyze an air filled square resonator. It is a simple 2D structure enclosed by four PEC boundaries. In TLM region, the boundaries are set on TLM cell boundaries, while in MRTD region, they are set on E_y nodes (TE mode). The interface is placed along x direction as shown in Figure. 2.3. The excitation function is raised cosine function with a smooth half-sin distribution in both x and z directions. The time domain response has been sampled at a pre-selected TLM node.

As illustrated in Figure. 2.5 the result is reasonably smooth at the beginning while shows the instability after about 900 MRTD time steps. This instability probably comes from the improper mixture of E-field and H-field information during the data transferring between MRTD and TLM. Thus, it seems reasonable if we give a try to another TLM method, the Alternating Transmission Line Matrix method (ATLM), to see whether its time and space staggering scheme could improve the instability problem in the hybrid MRTD-TLM combination algorithm.

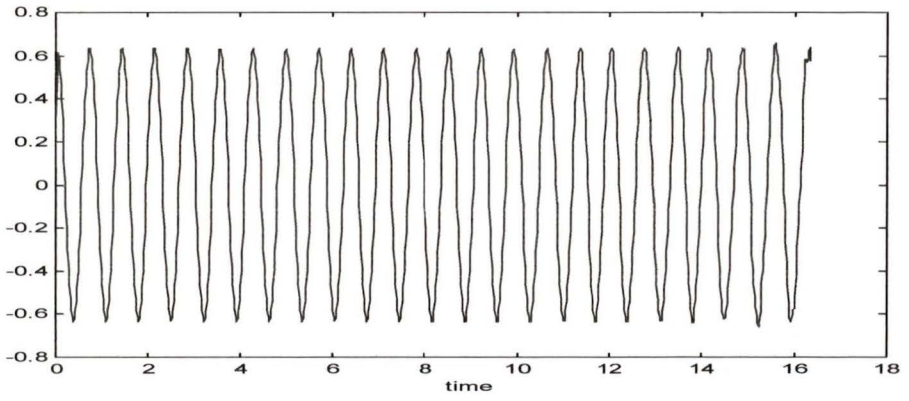

Figure. 2.5 Sampled time domain response: stable for about 900 MRTD time steps

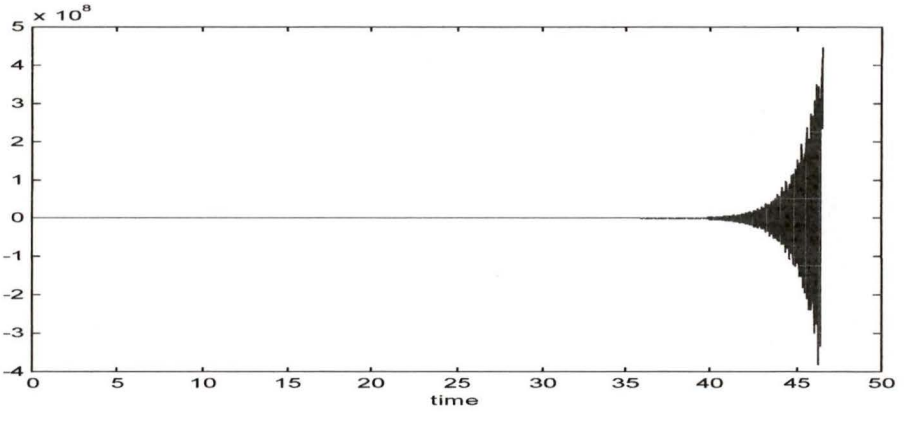

Figure. 2.6 Sampled time domain response: unstable after 900 MRTD time steps

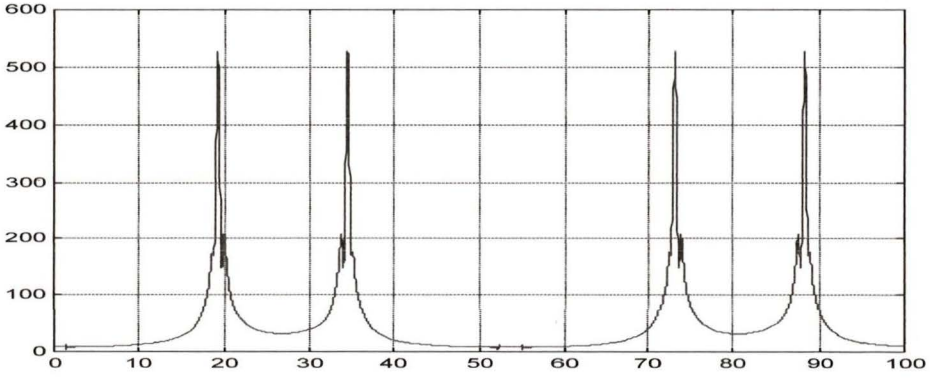

Figure. 2.7 Fourier transform of sampled time domain signals

Conclusion of this chapter will be included in next chapter after the discussion of hybrid ATLM - MRTD algorithm for the purpose of comparison.

Chapter 3 Hybrid Combination of ATLM and MRTD

3.1 Introduction

ATLM (Alternating TLM) is a scheme based on the TLM scheme for the symmetrical condensed node (SCN). The idea of ATLM is to reduce the numerical effort as well as storage requirement without major loss in accuracy by removing redundancy in the TLM algorithm. A parity p is introduced into the ATLM scheme [8]Russer and Bader. The discrete space coordinates i, j, k and the discrete time coordinate n are the same as in the regular TLM formulation.

$$p = \text{sign}(i + j + k + n) \tag{3.1}$$

If the sum $i+j+k+n$ is even then $p=+1$ and if $i+j+k+n$ is odd then $p=-1$. Hence, we separate all ATLM nodes into two sets: one set of even nodes with even parity, another of odd nodes with odd parity. At each time step, the process of scattering and connection must be performed on either the even or the odd set of nodes. This will not only reduce the computation time, but also decrease the chance of instability triggered by the presence of spurious solutions that can result from the interaction between the even and odd set of impulses introduced at boundaries and stubs.

The field theoretical derivation of ATLM is similar to that of the SCN. However, the two methods still differ in quite a few aspects.

Firstly, in TLM SCN, boundaries are introduced a cell boundaries half way between node centers. In ATLM, boundaries must be placed in the center of the cells.

Secondly, the sampling of ATLM field components is different from that of SCN: While in TLM with SCN, the field values in every three-dimensional cell with the spatial coordinates i, j, k are sampled at every time sampling point n in the cell boundaries, for ATLM, either the odd cells with odd $i+j+k+n$ or the even cells with even $i+j+k+n$ are sampled in the center of the three-dimensional cell. This sampling leads to a bijective mapping between the six field components, six spatial derivatives of the field components and the twelve wave amplitudes.

In the following sections a clear and easy-to-understand explanation of the basic concept of ATLM will be given. However, the detailed treatment of the ATLM scheme is rather complex and would exceed the scope of this thesis. The introduction of boundary conditions is included in section 3.3 and compared with the conventional TLM scheme. Details on ATLM can be found in the references given in the bibliography.

3.2 Concepts of ATLM

Figure. 3.1 shows that part of the impulse leaving a node comes back to the same node after one time step. This implies that in the traditional TLM scheme, there is a scattering and connection process happening for each node at each time step.

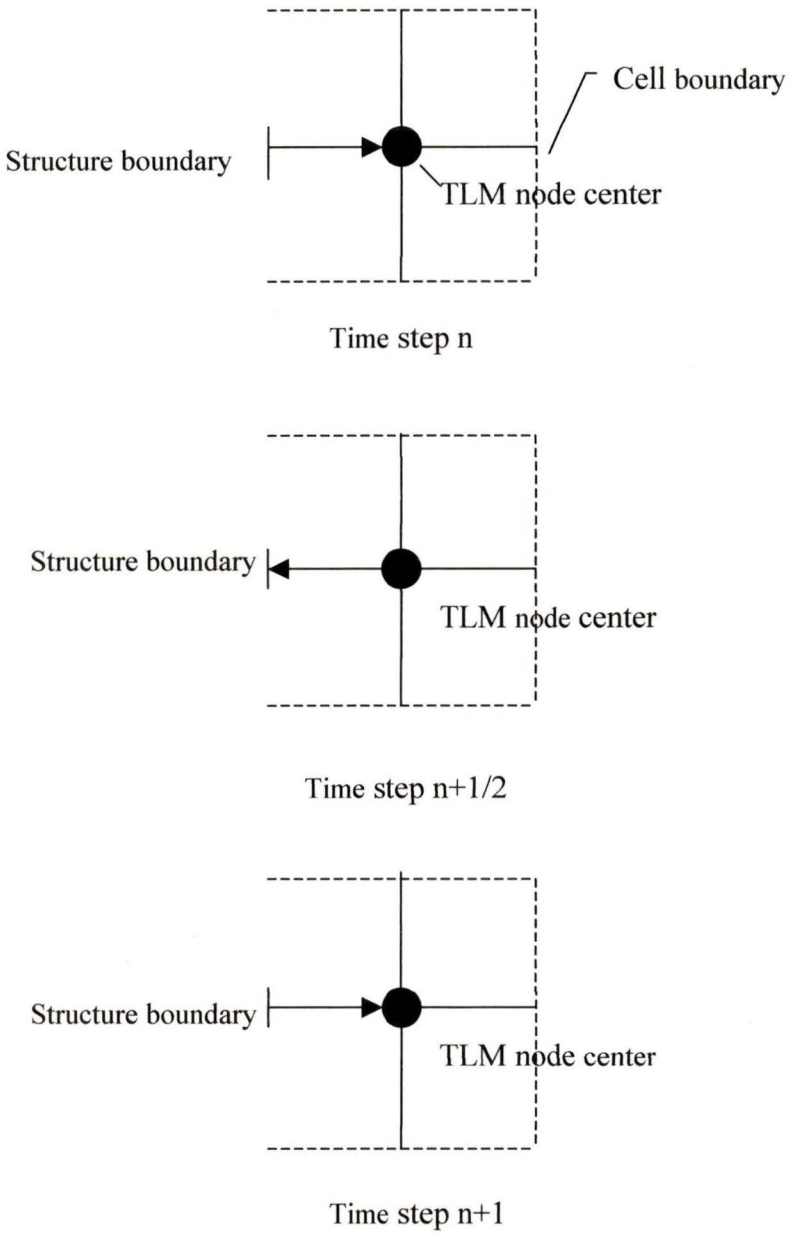

Figure. 3.1 Traditional TLM boundary setting and a single scattering process. If the boundary of a structure is replaced by the cell boundary of a neighboring node, the illustration still works, except that the reflected pulse includes the pulse incident from the other node.

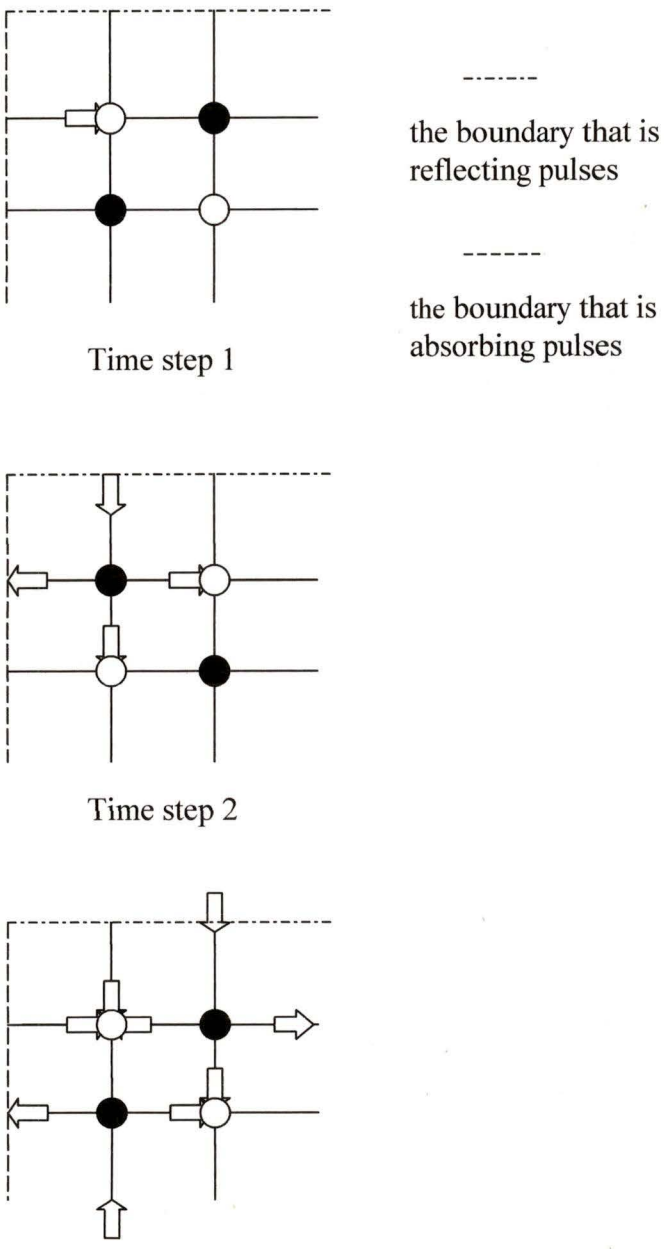

Figure. 3.2 Illustration on the wave pulse propagation in ATLM scheme.

Figure. 3.2 shows how the ATLM scheme works in a simple 2D TLM shunt network. Black and white nodes represent the different sets of nodes. At each time step, one set of

the nodes has even parity and the other has odd parity. If a single pulse is excited on one node as depicted in Figure. 3.2, the scattering process only occurs on one set of nodes at each time step. The boundary location prevents the scattering process on neighboring nodes from happening at the same time step.

Let us investigate what will happen when one node is continuously excited? Figure. 3.3 gives an explanation.

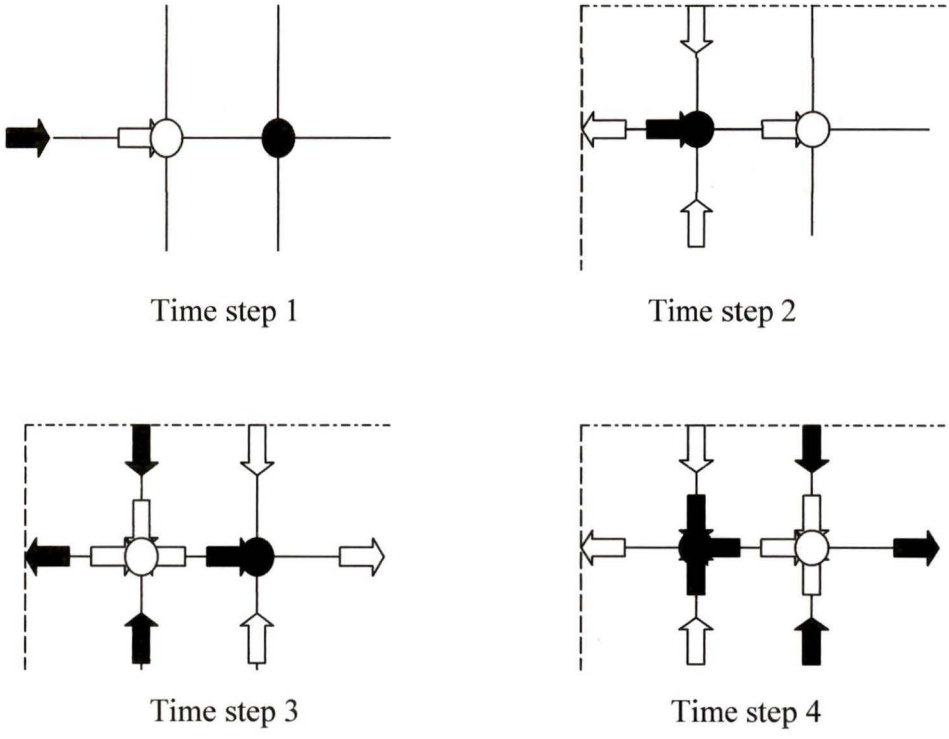

Figure. 3.3 Illustration of the wave pulse propagation in the ATLM scheme when one node is continuously excited

Obviously, in this case the two sets of pulses will not mix either.

A more complicated case is given in Figure. 3.4. It shows the behavior of the TLM network when the two neighboring nodes are excited at the same time step.

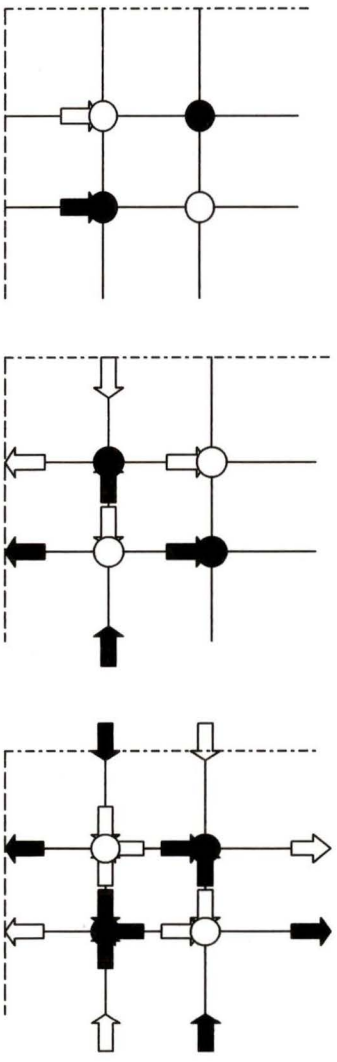

Figure. 3.4 Illustration of the wave pulse propagation in the ATLM scheme when two neighboring nodes are excited at the same time step

Figure. 3.4 shows that when the two sets of nodes are excited at the same time, the pulses, depicted with different color, again will not mix. Up to now, the discussion has been limited to the case of single pulse excitation. However, if the excitation continues for subsequent time steps, the pulse excited on the even set of nodes at the first time step is mixed with the pulse excited on odd set of nodes at the next time step, and vice versa.

From the above illustrations on the ATLM network, we may conclude that in the combination scheme of ATLM and MRTD, the excitation should always take place on staggered nodes, and none of the ATLM nodes should be excited at successive time steps to prevent the mixture of pulses from different set of nodes.

3.3 Hybrid ATLM-MRTD Scheme

In the hybrid ATLM-MRTD scheme, the boundary location in the MRTD region must be shifted by one quarter MRTD cell size away from the node center in accordance with the change in boundary position imposed by ATLM. The boundary conditions for MRTD region are also rewritten as (3.2). The derivation of these conditions is similar to that of the boundary condition in the TLM-MRTD scheme, hence, in this section it will not be given again. The notations E_0 and E_1 are as defined in the previous chapter.

$$
\begin{aligned}
&Upper \quad PEC && \begin{cases} E_0^{\phi\phi} = (E_1^{\phi\phi} - E_1^{\psi\phi})/4 \\ E_0^{\phi\psi} = (E_1^{\phi\psi} - E_1^{\psi\psi})/4 \\ E_0^{\psi\phi} = (E_1^{\phi\phi} - E_1^{\psi\phi})/4 \\ E_0^{\psi\psi} = (E_1^{\phi\psi} - E_1^{\psi\psi})/4 \end{cases} \\
&Lower \quad PEC && \begin{cases} E_0^{\phi\phi} = (E_1^{\phi\phi} + E_1^{\psi\phi})/4 \\ E_0^{\phi\psi} = (E_1^{\phi\psi} + E_1^{\psi\psi})/4 \\ E_0^{\psi\phi} = -(E_1^{\phi\phi} + E_1^{\psi\phi})/4 \\ E_0^{\psi\psi} = -(E_1^{\phi\psi} + E_1^{\psi\psi})/4 \end{cases} \\
&Right \quad PEC && \begin{cases} E_0^{\phi\phi} = (E_1^{\phi\phi} - E_1^{\phi\psi})/4 \\ E_0^{\phi\psi} = (E_1^{\phi\phi} - E_1^{\phi\psi})/4 \\ E_0^{\psi\phi} = (E_1^{\psi\phi} - E_1^{\psi\psi})/4 \\ E_0^{\psi\psi} = (E_1^{\psi\phi} - E_1^{\psi\psi})/4 \end{cases} \\
&Left \quad PEC && \begin{cases} E_0^{\phi\phi} = (E_1^{\phi\phi} + E_1^{\phi\psi})/4 \\ E_0^{\phi\psi} = -(E_1^{\phi\phi} + E_1^{\phi\psi})/4 \\ E_0^{\psi\phi} = (E_1^{\psi\phi} + E_1^{\psi\psi})/4 \\ E_0^{\psi\psi} = -(E_1^{\psi\phi} + E_1^{\psi\psi})/4 \end{cases}
\end{aligned}
\tag{3.2}
$$

3.4 Numerical Validation

The ATLM-MRTD algorithm is similar to the hybrid combination of TLM with MRTD. Only the difference between the two schemes will be specified in this section.

First, the ATLM region is excited at every second ATLM time step alternatively on staggered nodes. In conventional TLM, the region is also excited at every second TLM time step, but all nodes are excited at the same time. In the MRTD region, the field is excited when the E values are updated, exactly as in the TLM-MRTD scheme.

An array is used to temporarily save the TLM node voltages at the previous time step in the overlap region. Because of the characteristics of ATLM, not every node in the TLM region will be updated at each (TLM) time step. Thus, this causes some difficulties in the updating process in the MRTD region. The temporary array has been used to solve this problem by storing the necessary information from the previous time step so that the future values $E_y, H_x,$ and H_z. can be predicted.

The simulation of the electromagnetic field in a square waveguide cavity is shown below:

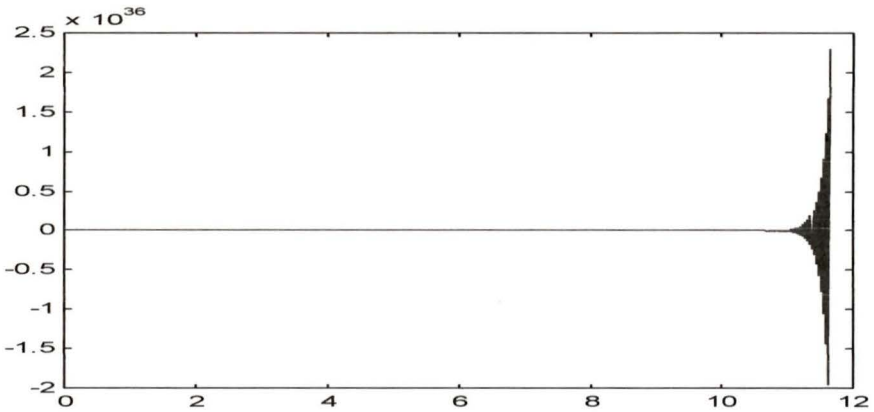

Figure. 3.5 Instability appears in the simulation result obtained with the ATLM-MRTD scheme

We see that the simulation performed with ATLM-MRTD becomes again unstable, even earlier than in the TLM-MRTD scheme. The cause for this worse result lies probably in the interpolation processes (process of rewriting E_y, H_x, H_z.).

More simulation results using the TLM-MRTD combination scheme can be found in the reference [3] and [4].

3.5 Conclusion of Part I

Two hybrid combination schemes have been derived, implemented and tested in this project: TLM-MRTD and ATLM-MRTD. The MRTD scheme employs Haar Wavelets as basis functions.

First, the traditional TLM network formulation was coupled to the MRTD algorithm. Formulas were derived for data transfer between two discretization sub-domains, reconstruction of field component values, extraction of the Haar wavelet coefficients, and update of E_y, H_x and H_z. The program was then applied to analyze a square waveguide cavity but the coupled algorithm was only stable for about 900 MRTD time steps.

Suspecting that this instability could be due to the improper mixture of electrical and magnetic field information during data transfer between MRTD and TLM regions, the ATLM scheme was introduced to improve stability. However, when the ATLM-MRTD scheme was applied to analyze the structure previously simulated with TLM-MRTD, instability occurred even earlier, making the problem worse.

Having excluded the mixing of the even and odd set of impulses in the TLM scheme as the cause of instability, we turned our attention to the differences in numerical dispersion as one of the reasons for instability in the hybrid scheme. Fig. 2.7 shows some unexpected frequency components in the result, and it may become necessary to introduce digital filters in the data connection between TLM and MRTD. More research will be required to fully understand and solve this instability problem.

PART II

Coupled TLM-Thermal Analysis

Chapter 4 Power Dissipation in Microwave Theory

4.1 Introduction

The dissipation of microwave power in objects placed into a waveguide leads to an increase in their temperature. The principal mechanisms of microwave power dissipation are the wall current losses in metallic boundaries and the volume current losses inside highly resistive dielectric materials [14]Pozar. Power dissipated in both metallic boundaries and dielectric objects are used as the source of heat distribution for the thermal analysis. The goal of this chapter is to determine the power absorbed by the metallic and dielectric objects when placed into the waveguide structure. For this purpose, the electromagnetic field inside the dielectric objects and at the surfaces of the waveguide must first be solved using an appropriate field simulation algorithm, such as the GSCN 3D TLM method.

4.2 Perfect Conductor

A perfect conductor is an idealized medium within which the electric field is always equal to zero. A good conductor is generally a medium whose conductivity, σ, is large. Therefore, it seems appropriate to define a perfect conductor as a medium whose conductivity is infinite.

The conditions $\sigma \to \infty$ and $E = 0$ can be considered equivalent to each other. Considering the power consumed in a volume V inside a conductor, it is given by

$$\int_v \sigma E^2 dv \tag{4.1}$$

If σ reaches infinity while E remains finite, the power consumption must also approach infinity. However, since any realistic power source can deliver only a finite amount of power, it seems appropriate to assume that the conditions $\sigma \to \infty$ correspond to $E = 0$ in ordinary cases. Furthermore, the amplitude of a plane wave diminishes quickly as it penetrates into a conductor, and as σ increases the attenuation becomes so large that an electromagnetic field inside a good conductor must become negligibly small. In the limit as $\sigma \to \infty$, the field must be zero.

4.3 Power Absorbed by Good Conductors and Dielectric Objects

4.3.1 Poynting's Theorem

Poynting's theorem (4.2), named after the physicist J.H. Poynting, is basically a power balance equation. It expresses the energy conservation for electromagnetic fields and sources.

$$\begin{aligned} &-\frac{1}{2}\int_v \left(\overline{E}\cdot\overline{J}_s^* + \overline{H}^*\cdot\overline{M}_s\right)dv \\ &= \frac{1}{2}\oint_S \overline{E}\times\overline{H}^*\cdot d\overline{s} + \frac{\sigma}{2}\int_v |\overline{E}|^2 dv + \frac{\omega}{2}\int_v \left(\varepsilon''|\overline{E}|^2 + \mu''|\overline{H}|^2\right)dv + j\frac{\omega}{2}\int_v \left(\mu'|\overline{H}|^2 - \varepsilon'|\overline{E}|^2\right)dv \end{aligned} \tag{4.2}$$

The integral on the left-hand side represents the complex power, P_s, delivered by the sources, $\overline{J}_s$ and $\overline{M}_s$, inside S:

$$P_s = -\frac{1}{2}\int_v \left(\overline{E}\cdot\overline{J}_s^* + \overline{H}^*\cdot\overline{M}_s\right)dv \tag{4.3}$$

The first integral on the right-hand side of (4.2) represents the complex power flow out of the closed surface S. If we define a quantity called the Poynting vector, $\overline{S}$, as

$$\overline{S} = \overline{E}\times\overline{H}^* \tag{4.4}$$

then this power can be expressed as

$$P_o = \frac{1}{2}\oint_S \overline{E}\times\overline{H}^*\cdot d\overline{s} = \frac{1}{2}\oint_S \overline{S}\cdot d\overline{s} \tag{4.5}$$

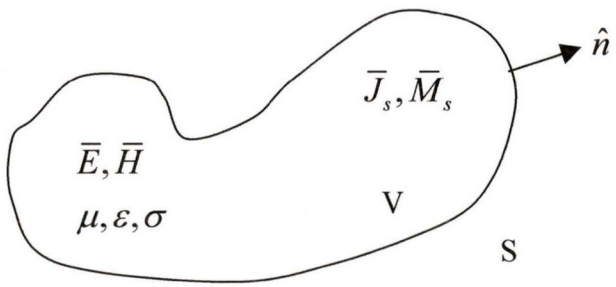

Figure. 4.1 A volume V, enclosed by the closed surface S, containing fields $\overline{E}$, $\overline{H}$, and current sources $\overline{J_s}$, $\overline{M_s}$.

The surface S in (4.5) must be a closed surface in order for this interpretation to be valid. The real parts of P_s and P_o in (4.3) and (4.5) represent time-average powers.

The second and third integrals in (4.2) are real quantities representing the time-average power dissipated in volume V due to conductivity, dielectric, and magnetic losses. If we define this power as P_l we have:

$$P_l = \frac{\sigma}{2}\int_V |\bar{E}|^2 \, d\upsilon + \frac{\omega}{2}\int_V \left(\varepsilon'' |\bar{E}|^2 + \mu'' |\bar{H}|^2\right) d\upsilon \tag{4.6}$$

which is sometimes referred to as Joule's law. The last integral in (4.2) represents the stored electric and magnetic energies.

With the above definitions, Poynting's theorem can be rewritten as

$$P_s = P_o + P_l + 2j\omega\left(W_m - W_e\right) \tag{4.7}$$

This complex power balance equation states that the power delivered by the sources (P_s) is equal to the sum of the power transmitted through the surface (P_o), the power lost to heat in the volume (P_l), and 2ω times the net reactive energy stored in the volume.

4.3.2 Power Absorbed by a Good Conductor

To calculate the losses in the walls of waveguides of relatively large but finite conductivity, it is usually assumed that the disturbance of the electric and the magnetic fields due to wall losses is so small that it can be neglected, and the field equations for zero wall losses are still valid. The losses due to wall currents are a function of the magnetic fields at the guide-wall surfaces if the influence of the electric field penetration into the wall is neglected.

The varying magnetic field immediately adjacent to the wall induces current in the wall, the density of which at the surface can be calculated from the boundary conditions. Owing to the imperfect conductivity of the wall, this current density creates an electric field E_w along the wall in the direction of the current density vector and hence perpendicular to the magnetic field H_w. These fields together give rise to a Poynting vector S_w perpendicular to the wall. Thus, some power P_w flows into the wall as well.

To find the power dissipated in the conductor of finite conductivity, consider the geometry of Figure. 4.2 below, which shows the interface between a lossless medium and a good conductor.

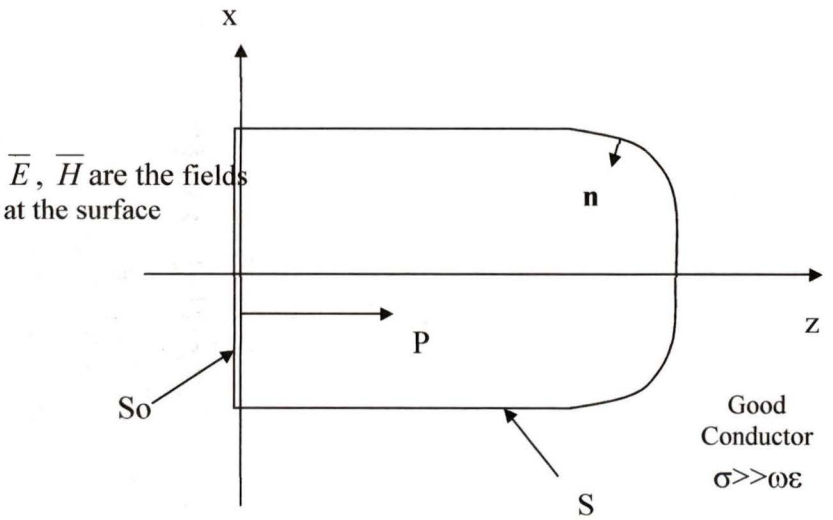

Figure. 4.2 Illustration on the calculation of power dissipation in good conductor

We assume that a field is incident from $z<0$ and that the field penetrates into the conducting region $z>0$. The real average power entering the conductor volume defined by the cross-sectional surface S_0 at the interface and the surface S is given as

$$P_{av}=\frac{1}{2}\int_{S_0+S}\overline{E}\times\overline{H}^{*}\cdot\hat{n}ds \tag{4.8}$$

where $\hat{n}$ is a unit normal vector pointing into the closed surface S_0+S, and $\overline{E}$, $\overline{H}$ are the fields at this surface. The contribution to the integral in (4.8) from the surface S can be made zero by proper selection on this surface. For example, if the field is a normally incident plane wave, the Poynting vector $\overline{S}=\overline{E}\times\overline{H}^{*}$ will be in the $\hat{z}$ direction, and so tangential to the top, bottom, front, and back of S, if these walls are made parallel to the z-axis. If the wave is obliquely incident, these walls can be slanted to obtain the same result. In addition, if the conductor is good, the decay of the fields from the interface at $z=0$ will be very rapid, so that the right-hand end of S can be made far enough away from $z=0$ so that there is negligible contribution to the integral from this part of the surface S. The power entering the conductor through S_0 can then be written as

$$P_{av}=\frac{1}{2}\mathrm{Re}\int_{S_0}\overline{E}\times\overline{H}^{*}\cdot\hat{z}ds \tag{4.9}$$

From the vector identities, we have

$$\hat{z}\cdot\left(\overline{E}\times\overline{H}^{*}\right)=\left(\hat{z}\times\overline{E}\right)\cdot\overline{H}^{*}=\eta\overline{H}\cdot\overline{H}^{*} \tag{4.10}$$

Where η is the wave impedance defined by the quotient of the amplitudes of the electric and the magnetic fields. For the particular case of a plane wave it can be written as

$$\eta = \sqrt{\frac{j\omega\mu}{\sigma + j\omega\varepsilon}} \tag{4.11}$$

For a good conductor $\sigma >> \omega\varepsilon$ (μ and σ representing respectively the permittivity and electric conductivity of the conductor) η reduces to

$$\eta \approx \sqrt{\frac{j\omega\mu}{\sigma}} = (1+j)\sqrt{\frac{\omega\mu}{2\sigma}} \tag{4.12}$$

The average power lost in the conductor P_{av} can be written as

$$P_{av} = \frac{R_s}{2}\int_{S_0} \left|\bar{H}\right|^2 ds \tag{4.13}$$

where

$$R_s = \mathrm{Re}(\eta) = \mathrm{Re}\left[(1+j)\sqrt{\frac{\omega\mu}{2\sigma}}\right] = \sqrt{\frac{\omega\mu}{2\sigma}} \tag{4.14}$$

The surface resistivity R_s of the conductor is the real part of its wave impedance as explained in the next section.

4.3.3 Modeling of Lossy Conducting Walls in the TLM Method

The wave impedance inside an imperfect conductor is

$$\eta_c = \sqrt{\frac{\mu_c \omega}{2\sigma_c}}(1+j) \tag{4.15}$$

where $\mu_c = \mu_0 \mu_{cr}$ and σ_c are the permeability and conductivity of the conductor. Since in a good conductor the penetration depth is very small, it is convenient to represent the boundary by a surface of impedance η_c. For good conductors, η_c is usually much smaller than η_0, and the imaginary part of the boundary reflection coefficient can be ignored. The impulse reflection coefficient terminating the TLM mesh thus becomes in the case of 2D TLM:

$$\Gamma_i = \frac{\eta_c - \eta_0\sqrt{2}}{\eta_c + \eta_0\sqrt{2}} = \frac{\frac{1}{2}\sqrt{(\mu_c\omega\varepsilon_0)/(\sigma_c\mu_0)}(1+j)-1}{\frac{1}{2}\sqrt{(\mu_c\omega\varepsilon_0)/(\sigma_c\mu_0)}(1+j)+1} : \; -1+\sqrt{\frac{\mu_c\omega\varepsilon_0}{\sigma\mu_0}} \tag{4.16}$$

In the case of 3D TLM,

$$\Gamma_i = \frac{\eta_c - \eta_0}{\eta_c + \eta_0} = \frac{\frac{1}{\sqrt{2}}\sqrt{(\mu_c\omega\varepsilon_0)/(\sigma_c\mu_0)}(1+j)-1}{\frac{1}{\sqrt{2}}\sqrt{(\mu_c\omega\varepsilon_0)/(\sigma_c\mu_0)}(1+j)+1} \tag{4.17}$$

Since Γ_i depends on the angular frequency ω, the TLM results are accurate only for that frequency which has been selected in determining Γ_i. Thus, this method of modeling losses in good conductors is acceptable for narrowband application. The field solution at that frequency can be extracted from the impulse response through Fourier transform.

4.4 Power Handling Capability

The average power handling capability of a waveguide is determined by the temperature rise of the waveguide in an air environment. The parameters that play major roles in the calculation of average power capacity are (a) attenuation in the guide, (b) surface area of the guide, (c) maximum tolerable temperature rise, and (d) ambient temperature (i.e., the temperature of the medium surrounding the inner and outer walls of the guide. Thus the average power rating can be raised if desired, by choosing a higher temperature limit and using forced cooling or cooling fins.

The approach to determining the average power rating is to find the attenuation per unit length. With the attenuation known, the dissipated power in the walls of the matched waveguide may be found when a given power is being transmitted through it. The dissipated power is then related to the rate of heat transfer from the waveguide walls to obtain the power rating of the waveguide.

The formula for the attenuation ([17] King and [24] Ragan) of an air-filled copper rectangular waveguide (TE_{10} mode) at a temperature of 20 °C is

$$\alpha = \frac{3.8649(10^{-5})\dfrac{\lambda}{\lambda_c}\left[\dfrac{a}{2b}+\left(\dfrac{\lambda}{\lambda_c}\right)^2\right]}{\lambda^{3/2}\sqrt{1-\left(\dfrac{\lambda}{\lambda_c}\right)^2}} \text{ db/m} \qquad (4.18)$$

where

a = the wide inner dimension of the waveguide in meters,

b = the narrow inner dimension of the waveguide in meters,

λ = the wavelength in meters, and

$\lambda_c = 2a$.

The attenuation, in terms of the power levels in the waveguide, is

$$\alpha = 4.34 \frac{P_l}{P_1} \text{db/unit length} \tag{4.19}$$

where

P_1 = power input, or the power rating of the waveguide, and

P_l = power loss in the unit length of the waveguide.

P_l is equivalent to the rate of heat transfer q from a unit length of the waveguide, and is related by $P_l = 0.293q$. Thus, the average power rating of the waveguide is

$$P_1 = \frac{1.271q}{\alpha} \tag{4.20}$$

The rate of heat transfer is the sum of the heat transferred by thermal conduction q_{cond}, thermal convection (q_{conv}) and thermal radiation (q_{rad}); that is:

$$q = q_{cond} + q_{conv} + q_{rad} \quad \text{(watts)} \tag{4.21}$$

4.5 Conclusion

First, the energy conservation equation based on Poynting's theory, is introduced. Then, the dissipation of power in good conductors and dielectric components is discussed. The power handling capability and attenuation coefficient are defined at the end of this chapter.

Chapter 5 Thermal Conduction

5.1 Introduction

Three mechanism of heat transfer, namely heat conduction, heat convection and heat radiation will be introduced in the next three chapters. Governing formulas will be introduced and relative derivation will be included. For more details of the background research, [19]-[29] are some good references for use.

Heat conduction is the term applied to the mechanism of internal energy exchange from one body to another, or from one part of a body to another. Conduction heat is transferred by the exchange of the kinetic energy of motion of the molecules or by the drift of free electrons in the case of heat conduction in metals. Heat conduction takes place within the boundaries of a body, or across the boundary of a body into another body placed in contact with the first. The laws governing conduction can be expressed in concise mathematical terms, and the analysis of the heat flow can be treated analytically in many instances.

5.2 Definition of Importance in General Heat Transfer

5.2.1 Specific Heat

The term "specific heat" expresses the variation in temperature of a material with the amount of heat stored in it. Most heat transfer processes occur at virtually constant pressure; hence, the constant pressure specific heat, C_p, is invariably used. The dimension of C_p is energy per unit mass per unit temperature change. In the SI system the units usually employed are kJ/kg·°C.

For solids and liquids, the specific heat is virtually independent of pressure until extremely high pressures are encountered. Hence for ordinary engineering applications any pressure effect may be ignored. Even the temperature dependence of C_p is slight for solids and liquids.

However, in the case of gases, the temperature dependence of the specific heat is much more pronounced than in the case of solids and liquids. A dependence on pressure is also sometimes present, but for gases far removed from saturation or the critical point, this dependence may often be ignored. In general, the higher the temperature, the less the effect of pressure.

5.3 Definition of Importance in Heat Conduction

5.3.1 Thermal Conductivity of Homogeneous Materials

As mentioned above, heat conduction is basically the transmission of energy by molecular motion. Thermal conductivity is then the physical property denoting the ease with which a particular substance can accomplish this transmission. The thermal

conductivity of a material is found to depend on the chemical composition of the substance, or substances, of which it is composed; on the phase in which it exists; on its crystalline structure if a solid; on the temperature and pressure to which it is subjected; and on whether or not it is a homogeneous material. A vast range of possible values of thermal conductivity exist in the material world with silver having a conductivity almost 50,000 times greater than that of Freon.

Generally speaking, a liquid is a better heat conductor than a gas and a solid is a better heat conductor than a liquid. These differences can be explained partially by the fact that while in a gaseous state, the molecules of a substance are spaced relatively far apart and their motion is random. This means that energy transfer by molecular impact is much slower than in the case of a liquid, in which the motion is still random but in which the molecules are more closely packed. The same is true concerning the difference between the thermal conductivity of the liquid and solid phases.

Many factors are known to influence the thermal conductivity of metals. The factors with the greatest influence are the chemical composition, phase change, and temperature. Usually there are very few materials affected by the first two factors and hence, only the temperature effect has to be accounted for.

It is known that the thermal conductivity of metals is directly proportional to the absolute temperature and the mean free path of the molecules. It has been observed that pure metals generally have thermal conductivities which decrease with temperature, but the presence of impurities or alloying elements, even in minute amounts, may reverse this trend.

It is usually possible to represent the temperature dependence of the thermal conductivity of a metal by a linear relation of the form $k = k_0(1+bt)$, in which k_0 is the thermal conductivity at $t = 0°C$ and b is a constant.

The thermal conductivity of gases increases with increasing temperature and is relatively independent of pressure if the pressure is near atmosphere pressure.

5.3.2 Thermal diffusivity

The property of thermal diffusivity is defined as:

$$\alpha = \frac{k}{\rho C_p} \tag{5.1}$$

where k and C_p are discussed above and ρ is the density of the substance. The units to be used for α are m^2/s. Since α involves the density, ρ, it may be quite pressure dependent for gases even though k and C_p are not.

5.4 Governing Law and Heat Conduction Equations

5.4.1 Fourier's law

The basic law governing heat conduction is Fourier's law. Given a plate of material having a surface area A and a thickness Δx, let one side be maintained at temperature T_1, uniformly over the surface, and the other side at temperature T_2. Let q denote the rate of heat flow through the plate, neglecting any edge effects. Experiment has shown that the rate of heat flow is directly proportional to the area A and the temperature

difference $T_1 - T_2$ but inversely proportional to the thickness Δx. This proportionality is denoted by k. Thus, Fourier's law is:

$$q = -kA\frac{T_1 - T_2}{\Delta x} \text{ [W]} \tag{5.2}$$

The constant of proportionality k is called the thermal conductivity of the material. It is a property dependent only on the composition of the material, not on its geometrical configuration.

5.4.2 General Heat Conduction Equation

In general a heat conduction problem consists of finding the temperature at any time and at any point within a specified solid which has been heated to a known initial temperature distribution and whose surface has been subjected to a known set of boundary conditions.

The general heat conduction equation governing this problem is

$$\rho C_p \frac{\partial T}{\partial t} = \nabla \cdot (k \nabla T) + q^* \tag{5.3}$$

where ρ is the density, C_p is the constant pressure specific heat, and q^* is the rate at which heat is being internally generated per unit of volume.

If the conductivity is treated as constant, and no internal source of energy is involved, the following form is obtained

$$\frac{\partial T}{\partial t} = \alpha \nabla^2 T \tag{5.4}$$

where α is the previously defined thermal diffusivity.

The steady state is defined in heat transfer as the condition which prevails in a heat conducting body when temperatures at fixed points do not change in time. In this case, the heat conduction equation reduces to Laplace's equation. In rectangular coordinates this is

$$\frac{\partial^2 T}{\partial x^2}+\frac{\partial^2 T}{\partial y^2}+\frac{\partial^2 T}{\partial z^2}=0 \tag{5.5}$$

The nonsteady conduction equation is

$$k(\frac{\partial^2 T}{\partial x^2}+\frac{\partial^2 T}{\partial y^2}+\frac{\partial^2 T}{\partial z^2})=\rho C_p \frac{\partial T}{\partial t} \tag{5.6}$$

Each side of the conduction equation in (5.6) represents the time rate of heat storage per unit volume at a point. Equation (5.6) is the basic formula for the transient simulation of thermal conduction in a case where no internal heat source is present. The next section will elaborate the numerical methods for the modeling of heat conduction based on (5.6).

5.5 Numerical Methods for Heat Conduction

Although a great number of problems have been solved analytically, only a limited number of relatively simple geometrical shapes can be handled. Also, only those boundary conditions that can be easily mathematically expressed may usually be applied. There are many heat conduction problems of considerable practical value for which no analytical solution is feasible. These problems usually involve geometrical shapes of a mathematically inconvenient sort. Thus, numerical approaches must be developed.

The various numerical methods all yield numerical values for temperatures at selected, discrete, points within the body being considered and only at discrete time intervals. Thus answers are obtained only for a given set of conditions, a given set of discrete points and discrete time intervals.

The numerical method presented here is based on the representation of the derivatives in the heat conduction equation by finite difference approximations.

5.5.1 Finite Difference Approximations

The relation of the finite difference expression to the differential equation can be understood best by deriving the latter from the former, via the use of a Taylor's expansion. Consider a function of two independent variables:

$$f = f(\xi, \eta) \tag{5.7}$$

Let h_1 represent an increment in the variable ξ. A forward expansion of the function at $\xi = \xi + h_1, \eta = \eta$, in terms of its value at $\xi = \xi, \eta = \eta$, is

$$f(\xi + h_1, \eta) = f(\xi, \eta) + h_1 \left(\frac{\partial f}{\partial \xi} \right)_{\xi,\eta} + \frac{h_1^2}{2} \left(\frac{\partial^2 f}{\partial \xi^2} \right)_{\xi,\eta} + \frac{h_1^3}{6} \left(\frac{\partial^3 f}{\partial \xi^3} \right)_{\xi,\eta} + \vartheta(h_1^4) \tag{5.8}$$

The notation $\vartheta(h_1^4)$ is used to indicate that subsequent terms are of the order of h_1^4, and higher. If terms of the order of h_1^2, and greater, are neglected, the following forward difference approximation to the first derivative is obtained:

$$\left[\left(\frac{\partial f}{\partial \xi}\right)_{\xi,\eta}\right]_{fwd} \approx \frac{1}{h_1}\left[f(\xi+h_1,\eta)-f(\xi,\eta)\right] \tag{5.9}$$

For a forward displacement of h_2 in η, the forward finite difference approximation for the first derivative is

$$\left[\left(\frac{\partial f}{\partial \eta}\right)_{\xi,\eta}\right]_{fwd} \approx \frac{1}{h_2}\left[f(\xi,\eta+h_2)-f(\xi,\eta)\right] \tag{5.10}$$

Similarly, backward finite difference expressions for the first derivatives may be obtained by writing Taylor's expansions for an increment in ξ of $-h_1$ or an increment in η of $-h_2$:

$$f(\xi-h_1,\eta) = f(\xi,\eta) - h_1\left(\frac{\partial f}{\partial \xi}\right)_{\xi,\eta} + \frac{h_1^2}{2}\left(\frac{\partial^2 f}{\partial \xi^2}\right)_{\xi,\eta} - \frac{h_1^3}{6}\left(\frac{\partial^3 f}{\partial \xi^3}\right)_{\xi,\eta} + \vartheta(h_1^4) \tag{5.11}$$

Again neglecting terms of order h_1^2, and greater, one obtains

$$\left[\left(\frac{\partial f}{\partial \xi}\right)_{\xi,\eta}\right]_{bkwd} \approx \frac{1}{h_1}\left[f(\xi,\eta)-f(\xi-h_1,\eta)\right] \tag{5.12}$$

Also,

$$\left[\left(\frac{\partial f}{\partial \eta}\right)_{\xi,\eta}\right]_{bkwd} \approx \frac{1}{h_2}\left[f(\xi,\eta)-f(\xi,\eta-h_2)\right] \tag{5.13}$$

The central finite difference approximation to the second derivatives may be found by adding (5.8) and (5.11):

$$f(\xi+h_1,\eta)+f(\xi-h_1,\eta)=2f(\xi,\eta)+h_1^2\left(\frac{\partial^2 f}{\partial\xi^2}\right)_{\xi,\eta}+\vartheta(h_1^4) \tag{5.14}$$

When terms of the order of h_1^4, and greater, are neglected,

$$\left[\left(\frac{\partial^2 f}{\partial\xi^2}\right)_{\xi,\eta}\right]_{cent}\approx\frac{1}{h_1^2}\left[f(\xi+h_1,\eta)-2f(\xi,\eta)+f(\xi-h_1,\eta)\right] \tag{5.15}$$

Also,

$$\left[\left(\frac{\partial^2 f}{\partial\eta^2}\right)_{\xi,\eta}\right]_{cent}\approx\frac{1}{h_2^2}\left[f(\xi,\eta+h_2)-2f(\xi,\eta)+f(\xi,\eta-h_2)\right] \tag{5.16}$$

Other approximations to the second derivative may be written (e.g., forward, backward, etc.). However, the central difference given here is most commonly used for heat conduction analyses.

5.5.2 Numerical Methods for Modeling Transient Thermal Conduction

Of importance is the application of numerical techniques to the analysis of transient conduction problems. The difference between the steady and nonsteady cases lies in the finite difference representations that may be written for the partial derivative of temperature with respect to time. As discussed in the previous section, two possible finite difference expressions may be written for a first derivative, the forward difference and

the backward difference. These representations lead to two different numerical methods for transient problems: explicit and implicit formulations, respectively.

The advantage of the explicit representation is that the forward difference equation gives the future temperature of a single node in terms of current temperatures of that node and its neighbors. Thus, if at a certain time all the nodal temperatures are known, then each of the nodal temperatures at the end of the next time interval may be explicitly found, node by node. However, in the case of an implicit equation, the future nodal temperature is expressed in terms of a current value and the future values of its neighbors' temperatures, which brings difficulty to the iteration of calculating the nodal temperature at each node.

On the other hand, the disadvantage of the explicit representation is its restriction upon the magnitude of the time step Δt in relation to the spatial increment as will be elaborated in next section. Thus, the explicit formulation may actually involve more calculation time than the less-direct implicit method.

5.5.3 Stability Criteria

In transient modeling problems, the stability of the difference equations must be considered. Detailed analyses of the stability properties of the equations used for thermal conduction are quite complex, but simple stability criteria may be developed on an elementary basis.

As discussed earlier, the explicit formulation avoids the need for iterative or matrix inversion technique, since each future nodal temperature can be individually calculated for a time increment Δt from only the current nodal temperatures. For simplicity of

discussion, any internal heat generation has been considered zero. Assuming a uniform mesh is created with cell length Δl, then the explicit expression of future temperature at node i, T_i', in terms of the other quantities may be written as

$$T_i = T_i(1 - \sum_j \frac{\Delta t}{\Delta l^2 \cdot \alpha}) + \sum_j \frac{T_j \Delta t}{\Delta l^2 \cdot \alpha} \tag{5.17}$$

We see that new temperatures are successively calculated at each node starting with the given initial temperature distribution in a network for a given Δt. Time is then incremented and the calculations are repeated. No iterations or matrix inversions are required.

The stability condition for such a form is:

$$\sum_j \frac{\Delta t}{\Delta l^2 \cdot \alpha} \leq 1 \tag{5.18}$$

where j is the index of cells surrounding the cell i. The stability condition can be easily rewritten as:

$$\begin{aligned} &\text{One dimension}: \quad \Delta t \leq \frac{1}{2}\frac{(\Delta l)^2}{\alpha} \\ &\text{Two dimensions}: \Delta t \leq \frac{1}{4}\frac{(\Delta l)^2}{\alpha} \\ &\text{Three dimensions}: \quad \Delta t \leq \frac{1}{6}\frac{(\Delta l)^2}{\alpha} \end{aligned} \tag{5.19}$$

where α is the diffusivity.

5.5.4 Alternating Numerical Approach for Heat Conduction

A slightly modified finite difference scheme is presented by Halla and Wiesbeck[15] to model the conductive heat transfer in a rectangular uniform grid with cells indexed by (i, j, k). Inside a cell the temperature is assumed to be homogeneous. Heat flux density vectors describing the heat exchange with the neighboring cells are defined in the middle of the six cell surfaces as shown in Figure. 5.1 and for the discretization cell (i, j, k)

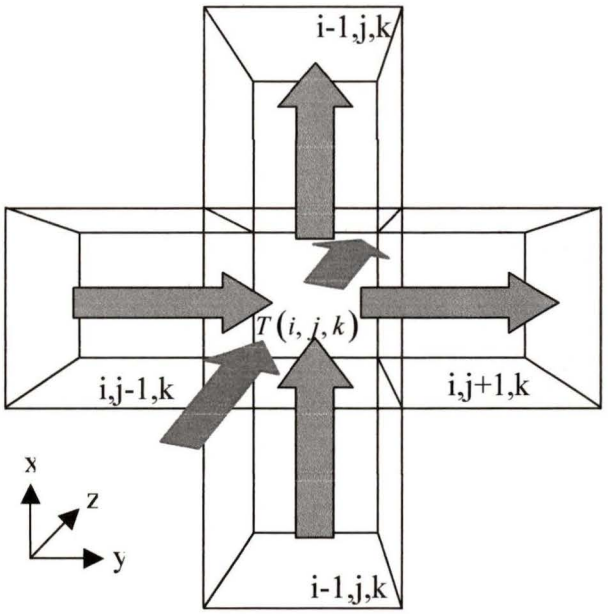

Figure. 5.1 Discretization cell (i, j, k) and the position of the scalar function values T and the vectors j

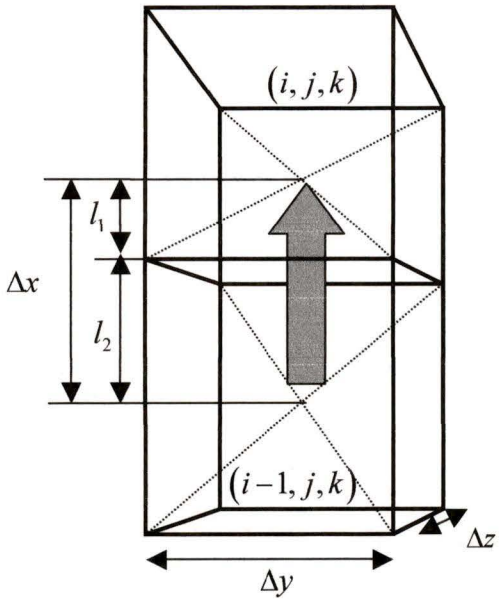

Figure. 5.2 Geometrical properties for the calculation of the discretized field component j_x

The calculation of the temperature distribution is divided into two steps. The conductive heat flux densities are caused by the temperature gradients between neighboring cells and are given by

$$\vec{j}(\vec{x},t) = -k(\vec{x},t)\,\mathrm{grad}\left(T(\vec{x},t)\right) \tag{5.20}$$

with $\vec{j}$ the heat flux density, and k the thermal conductivity. Considering only the x component of $\vec{j}$ in Figure. 5.1 as shown in Figure. 5.2 the gradient in (5.20) is expressed using the finite difference expression

$$\mathrm{grad}\left(T(\vec{x},t)\right) = \frac{T(i,j,k) - T(i-1,j,k)}{\Delta x} \tag{5.21}$$

The thermal conductivity at $\bar{x}$ is the average of two neighboring cells. In case of uniform mesh

$$k(\bar{x},t)=\Delta x\frac{k(i,j,k)k(i-1,j,k)}{k(i,j,k)l_2+k(i-1,j,k)l_1}=\frac{1}{2}\cdot\frac{k(i,j,k)k(i-1,j,k)}{k(i,j,k)+k(i-1,j,k)} \tag{5.22}$$

$$j_x(i,j,k)=\frac{1}{2}\cdot\frac{k(i,j,k)k(i-1,j,k)}{k(i,j,k)+k(i-1,j,k)}\left(T(i-1,j,k)-T(i,j,k)\right) \tag{5.23}$$

Note that in the above expression, k denotes thermal conductivity when it appears outside of the brackets. It denotes the index of the cell if it appears inside the brackets.

The thermal conductivity is assumed to be constant over the volume of one discretization cell. As the heat flux density is supposed to be constant over the surface, the power P_x flowing through the interface between the cells (i,j,k) and $(i-1,j,k)$ is determined by

$$P_x(i,j,k)=\iint_A j_x dA=j_x(i,j,k)\Delta x\Delta y \tag{5.24}$$

All other components of $\bar{j}$ and P are obtained accordingly.

When the conservation of energy

$$\operatorname{div}\bar{j}(\bar{x},T)+C_p(\bar{x},T)\rho(\bar{x},T)\frac{\Delta T(\bar{x})}{\Delta t}=0 \tag{5.25}$$

is applied to one cell (i,j,k) the divergence of $\bar{j}$ equals the power that flows through the surfaces of the cell. C_p and ρ are the specific heat and density, respectively. The

divergence of $\bar{j}$ is expressed by the discretised surface integral in equation (5.24). This leads to

$$\begin{aligned} &\operatorname{div} j(\bar{x}) \Rightarrow \oiint_A j(\bar{x})\, dA \\ &= P_x(i,j,k) - P_x(i+1,j,k) + P_y(i,j,k) \\ &-P_y(i,j+1,k) + P_z(i,j,k) - P_z(i,j,k+1) \end{aligned} \tag{5.26}$$

in the finite difference scheme.

The right hand side term in equation (5.25) applied to the cell volume leads to

$$\begin{aligned} C_p(\bar{x}.T)\,\rho(\bar{x},T)\frac{\Delta T(\bar{x},t)}{\Delta t} \Rightarrow \iiint_V C_p(\bar{x},T)\rho(\bar{x},T)\frac{\Delta T(\bar{x},t)}{\Delta t}\, dV \\ = \Delta x \Delta y \Delta z C_p(i,j,k)\,\rho(i,j,k)\frac{\Delta T(i,j,k)}{\Delta t} \end{aligned} \tag{5.27}$$

Finally the time derivative is also expressed by a finite difference

$$\frac{\partial T(\bar{x})}{\partial t} = \frac{T^{n+1}(i,j,k) - T^n(i,j,k)}{\Delta t} \tag{5.28}$$

where T^n denotes the temperature at time step n. Using equations (5.26), (5.27) and (5.28) one obtains

$$\begin{aligned} T^{n+1}(i,j,k) = T^n(i,j,k) + \frac{\Delta t}{\Delta x \Delta y \Delta z C_p(i,j,k)\,\rho(i,j,k)} \\ \left[P_x(i,j,k) - P_x(i+1,j,k) + P_y(i,j,k) - P_y(i,j+1,k) + P_z(i,j,k) - P_z(i,j,k+1)\right] \end{aligned} \tag{5.29}$$

With equation (5.29) and (5.24) the temperature is updated at each time step.

5.6 Conclusion

At the beginning of the chapter, the material properties of importance in general heat transfer and heat conduction are defined and explained. Then a FDTD representation of the differential heat conduction equation is derived. After the stability criteria are presented, an alternating FDTD formulation of heat conduction is described.

Chapter 6 Thermal Convection

6.1 Introduction

Convection is the term used to define the heat transfer mechanism which occurs in a fluid when one portion of the fluid mixes with another portion due to gross movements of the mass of fluid. The fluid motion may be caused by external mechanical means such as a fan, etc. In this case, the process is defined as forced convection. In the other case, the fluid motion is caused by density differences which are created by the temperature differences existing in the fluid mass. This process is termed free convection. The basic laws of heat conduction must be coupled with those of fluid motion in order to describe, mathematically, the process of heat convection.

6.2 Definitions of Interest in Thermal Convection

6.2.1 The coefficient of thermal expansion

The driving force in the process of free convection is the gravity acting on fluid regions of different density. These density differences result from temperature differences in the fluid regions. An important physical property of the fluid in this process is the coefficient of thermal expansion. Since the free convection process occurs only in liquids and gases,

the following discussion does not include the consideration of solids. The coefficient of thermal expansion is defined as

$$\beta = \frac{1}{V}\left(\frac{\partial V}{\partial t}\right)_p = -\frac{1}{\rho}\left(\frac{\partial \rho}{\partial t}\right)_p \tag{6.1}$$

where ρ is the fluid density, $V = \frac{1}{\rho}$ is the specific volume, and t is the temperature in $^{\circ}\mathrm{C}$.

For gases, the coefficient of expansion may be calculated from the definition in (6.1)if the following thermal equation of state holds

$$\rho = \mathrm{f}(P, T) \tag{6.2}$$

where P is the thermodynamic pressure, and T is the absolute temperature. For the ideal gas, application of (6.1) gives:

$$\beta = \frac{1}{T} \tag{6.3}$$

6.2.2 Dynamic Viscosity

Fluids, both gases and liquids, are observed to resist deformation in a manner which is proportional to the time rate of deformation. It is important to express the forces of resistance in terms of the velocity field of the fluid in the process of heat convection. The resistance to the shearing motion is the dominant resistive force and is expressed in terms of the fluid property known as viscosity.

According to Newton's definition of the dynamic viscosity coefficient, the shearing stress, τ, is directly proportional to the velocity gradient taken in a direction normal to the plane s which the fluid passes by.

$$\tau = \mu \frac{dv}{dn} \tag{6.4}$$

where μ, the constant of proportionality, is also termed the coefficient of dynamic viscosity, v is the fluid velocity, and n is the normal to the plane s. This definition applies only to laminar flow—not to turbulent flow, in which gross transverse fluctuations and mixing occur.

6.2.3 Kinematic Viscosity

Since the forces of viscosity act directly on a fluid, and since the fluid inertia resists these forces, the ratio of the viscous force to the inertia force is an important parameter in the analysis of fluid motion. Thus, the kinematic viscosity, defined as the ratio of the dynamic viscosity to the fluid density becomes an important fluid property. The kinematic viscosity is denoted by ν:

$$\nu = \frac{\mu}{\rho} \tag{6.5}$$

where μ is the constant of proportionality defined for dynamic viscosity, and ρ is the fluid density.

6.2.4 The Prandtl Number

In problems of convection one must consider the simultaneous exchange of momentum through viscosity and heat through conduction, where it is found that the ratio of the kinematic viscosity to the thermal diffusivity plays a significant role. This ratio is called the Prandtl Number and is purely a fluid property. The Prandtl number is defined:

$$P_r = \frac{\text{kinematic viscosity}}{\text{thermal diffusivity}} = \frac{\nu}{\alpha} = \frac{\mu C_p}{k} \tag{6.6}$$

Both ν and α have the dimensions of length^2/time; thus, P_r has no dimensions. The value of P_r is mainly dependent on temperature with little dependence on pressure.

6.3 Concept of Boundary Layer

When fluid moves past a solid surface, it is observed that the fluid velocity varies from a zero value immediately adjacent to the wall to a finite value at a point at a distance. This is mainly because the fluid particles adjacent to the surface tend to stick to it and therefore have zero velocity relative to the surface. In turn other fluid particles attempting to slide over the stationary ones at the surface are retarded as a result of viscous forces between the fluid particles.

For fluids of low viscosity (e.g. air), the region near the surface, in which most of the velocity variation occurs, may be quite thin so that in many applications it is possible to obtain satisfactory result by assuming that the fluid is inviscid and slips past the surface with no viscous retardation. However, since the process of convection of heat away from the wall is intimately concerned with thermal conduction and energy transport due to motion in the fluid layers in the immediate vicinity of the wall, the simplification of

assuming the fluid to be inviscid should not be made when analysis of heat convection is undertaken.

The velocity boundary layer is defined as the thin layer near the wall in which one assumes that viscous effects are important. Within this region the effect of the wall on the motion of the fluid is significant. Outside the boundary layer it is assumed that the effect of the wall may be neglected and the fluid is inviscid.

6.4 Laminar and Turbulent Flow

Inside the boundary layer the flow may be either laminar or turbulent as illustrated in Figure. 6.1

In the case of laminar boundary layer flow, adjacent fluid layers slide relative to one another but do not mix in the direction normal to the fluid velocity. Thus, any heat that flows from the surface to the inviscid fluid is done mostly by conduction

In the case of turbulent boundary layer flow, the mean flow is essentially parallel to the surface, but it has superimposed upon it a fluctuating motion in directions both parallel and normal to the surface. The transverse fluctuations cause additional fluid mixing, which increases the rate at which heat is transported in the direction normal to the surface.

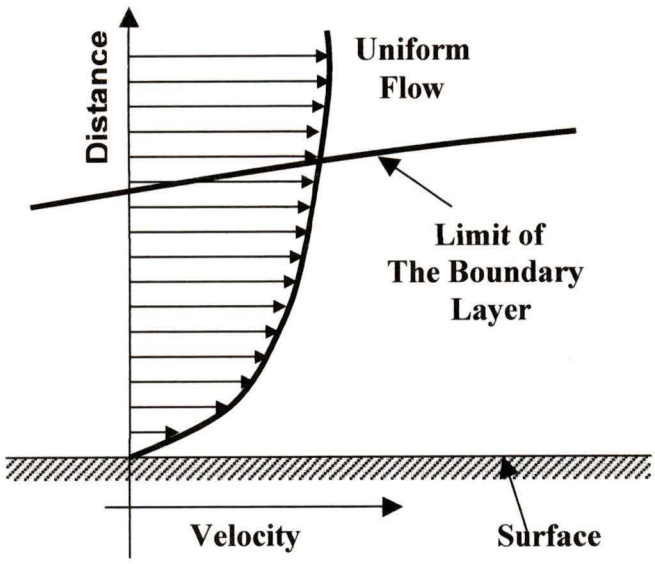

Laminar Boundary Layer

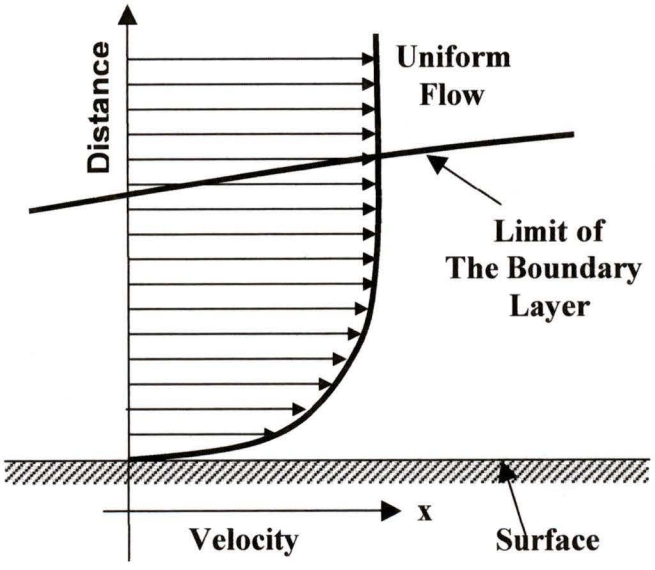

Turbulent Boundary Layer

Figure. 6.1 Illustration on the boundary layer concept: laminar and turbulent flow

6.5 Newton's law of cooling

As can be seen from the foregoing discussion, the prediction of the rates at which heat is convected away from a solid surface by an ambient fluid involves a thorough understanding of the principles of heat conduction, fluid dynamics, and boundary layer theory. All the complexities involved in such an analytical approach may be combined together in a single parameter, heat transfer coefficient h, introduced by Newton's law of cooling:

$$\frac{q}{A} = h(T_s - T_f) \tag{6.7}$$

The dimension of h is [W/(m^2·°K)]. T_s is the surface temperature and T_f is the fluid temperature.

The heat transfer coefficient is actually a complicated function of the flow conditions, thermophysical properties of the fluid (viscosity, thermal conductivity, specific heat, density), and the geometry and dimensions of the surface. In general, its numerical value is not uniform over the surface.

6.6 Free convection

In free or natural convection fluid velocity at points remote from the body will essentially be zero. Near the body there will be some fluid motion if the body is at a temperature different from that of the free fluid. If such is the case, there will be a density difference between the fluid near the surface and that which is far removed from the surface. This density difference will produce a positive or negative buoyant force in the fluid near the

surface(depending on whether the surface is hotter or colder than the fluid). The buoyant force results in a fluid motion, substantially in the vertical direction, past the surface—with consequent convective heat transfer taking place. The force of gravity is the driving force that produces the fluid motion and maintains the convective process.

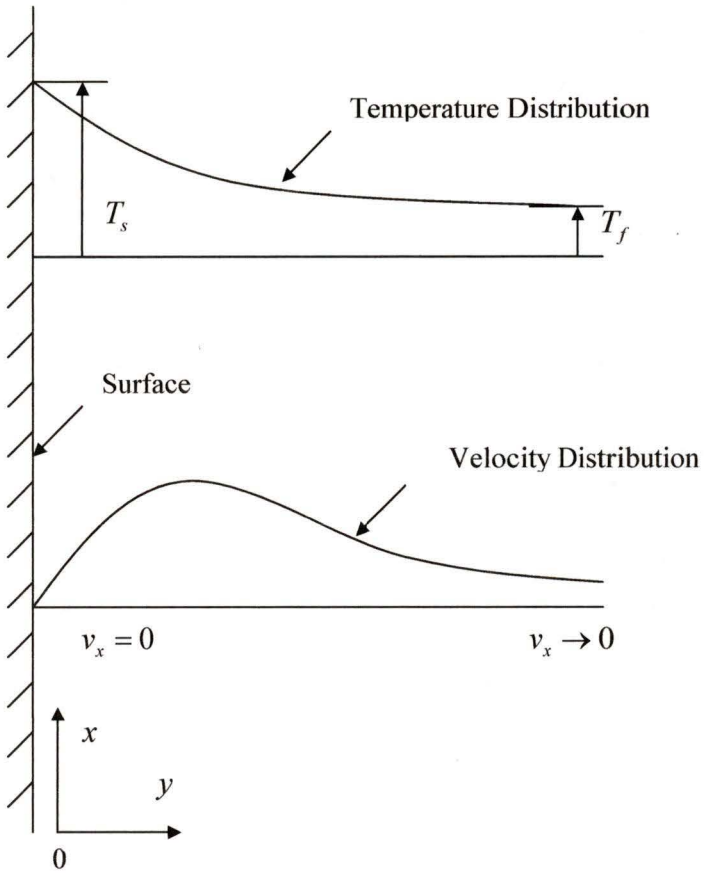

Figure. 6.2 Temperature and velocity distributions near a heated vertical surface in free convection flow

As illustrated in Figure. 6.2, if the wall temperature is higher than the fluid temperature immediately adjacent to it, the fluid velocity in the boundary layer retards the fluid out of the layer. In the region far away from the heated wall, the fluid temperature is near

uniform so that there is no density difference among the different parts of fluid mass. Thus, the velocity there again approaches zero.

The governing equation of free convection is written using the illustration in Figure. 6.2:

$$\frac{d}{dx}\int_0^\delta v_x^2 dy = \int_0^\delta g\beta(T-T_f)dy - \nu\left(\frac{\partial v_x}{\partial y}\right)_0 \tag{6.8}$$

with the boundary conditions

$$\begin{aligned} &\text{At y = 0:} \quad && T = T_s, v_x = 0 \\ &\text{At y = } \infty\text{:} \quad && T = T_f, v_x = 0 \end{aligned} \tag{6.9}$$

to be satisfied. Here δ is termed the boundary layer thickness and is observed as a function of x in many practical experiments. v_x is the fluid velocity component in x direction. g is the gravitational acceleration and β is the defined coefficient of thermal expansion.

The solution of the above equations along with some energy conservation conditions is complicated by the fact that the equations are coupled.

6.7 Evaluation of the heat transfer coefficient

As stated before, the analytical approach to the determination of the heat transfer coefficient would involve the finding of the temperature distribution in the fluid surrounding the body, which is almost prohibitively complex in some sense. Empirically the heat transfer coefficient may be approximately predicted and the computation simplified with the use of the following numbers. These numbers have been defined and

applied in all the heat transfer books and are important concepts in the analysis of the process of heat convection.

- The Nusselt number

The Nusselt number is interpreted as the temperature gradient at the surface:

$$Nu = \frac{hl}{k_f} \tag{6.10}$$

where h is the heat transfer coefficient, l is the characteristic length of the surface of interest which will be explained later in this section, and k_f is the fluid conductivity.

- The Grashof number

The Grashof number is interpreted as the ratio of buoyancy to viscous forces:

$$\mathrm{Gr} = \frac{l^3 g \beta \Delta T}{\nu^2} \tag{6.11}$$

where l is a characteristic length as above, ΔT is the surface-fluid temperature difference $(T_s - T_f)$, g is the gravitational acceleration, β is the coefficient of thermal expansion, and ν is the kinematic viscosity.

- The Rayleigh number

The Rayleigh number, Ra, is defined as

$$\begin{aligned} \mathrm{Ra} &= \mathrm{GrPr} \\ &= \frac{l^3 g \beta \Delta t \mathrm{Pr}}{\nu^2} \end{aligned} \tag{6.12}$$

It is simply the product of the previously defined Grashof and Prandtl numbers.

All free convection flow is not limited to laminar flow. In fact, most free convection flows arise from instabilities created by heated fluid rising past cooler fluid which must descend. Such disturbances may be amplified in the resultant boundary layers, and eventually, turbulence may be established. The laminar-turbulent transition depends on the relative magnitude of the buoyant forces and the resisting viscous forces as expressed through the Granshof or Rayleigh numbers. A detailed analysis of free convection stability is rather complex; however, as a general rule one may expect that transition will occur for a critical Rayleigh number of:

$$\mathrm{Ra}_{x,c} \cong 10^9 \tag{6.13}$$

- Evaluation of the Nusselt Number in Different Cases

The general prediction of the Nusselt Number is of the form:

$$\mathrm{Nu} = f(\mathrm{Gr},\mathrm{Pr}) \tag{6.14}$$

In terms of the Rayleigh number, the correlations for free convection would be expected to take the form:

$$\mathrm{Nu} = f(\mathrm{Ra},\mathrm{Pr}) \tag{6.15}$$

For the free convection around vertical plates, the following relation has been suggested and applied in most thermal application:

$$\mathrm{Nu_L} = 0.68 + 0.670\mathrm{Ra_L}^{1/4}\left[1+\left(\frac{0.492}{\mathrm{Pr}}\right)^{9/16}\right]^{-4/9}, \qquad 0 < \mathrm{Ra_L} < 10^9$$

$$\mathrm{Nu_L} = \left\{0.825 + 0.387\mathrm{Ra_L}^{1/6}\left[1+\left(\frac{0.492}{\mathrm{Pr}}\right)^{9/16}\right]^{-8/27}\right\}^2, 10^9 < \mathrm{Ra_L} \qquad (6.16)$$

$$\left[\begin{array}{l} 0 < \mathrm{Pr} < \infty \\ \text{properties, except } \beta, \text{ at } t_m \\ \beta \text{ at } t_m \text{ for liquids, at } t_f \text{ for gases} \end{array}\right]$$

Actually, the second of the above two equations may be applied over an entire range of Ra; however, better accuracy is obtained from the use of the first equation. The presence of the constant 0.68 results from the need at very low Ra, where the boundary layer approximations do not hold, to approach a nonzero value of Nu.

In the case of free convection around vertical surfaces, the flow produced by the free convection is parallel to the surface regardless of whether the surface was hotter or colder than the ambient fluid. However, in the case of free convection around heated or cooled horizontal plates, the principal body dimension is normal to the direction of the buoyant forces.

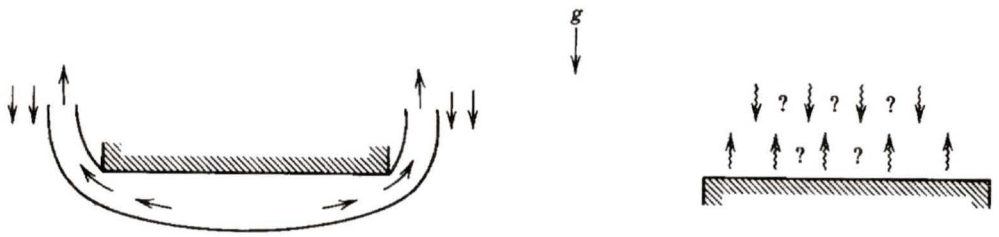

Figure. 6.3 Heated plates facing down (left) and facing up (right)

In the case of a heated plate facing down, as depicted in Figure. 6.3, the less dense, heated, fluid forms at the bottom surface of the plate and, seeking a way to rise, flows laterally to the edge and then up. A flow pattern, somewhat as sketched, is then established.

However, if the heated surfaces face up, as in Figure. 6.3, the less dense fluid forms on the top surface, and its tendency to rise is inhibited by the denser, cooler, fluid above it that tends to move down. Thus, in this case an unstable situation is created, and the exact nature of the flow pattern is strongly influenced by other effects such as possible small inclinations of the plate surface, the influence of fluid motion on the other side of the plate, etc.

Because of the above effects, reliable correlations for horizontal plates are difficult to find. Usually the following recommendations are made:

Characteristic length for horizontal surfaces is preferred as:

$$L_c = \frac{\text{plate area}}{\text{plate perimeter}} \tag{6.17}$$

As for the heated plate which is facing up or the cooled plate that is facing down, we have:

$$\begin{aligned} \mathrm{Nu}_{L_c} &= 0.54\mathrm{Ra}_{L_c}^{1/4}, \qquad 2.6\times10^4 < \mathrm{Ra}_{L_c} < 10^7 \\ \mathrm{Nu}_{L_c} &= 0.15\mathrm{Ra}_{L_c}^{1/3}, \qquad 10^7 < \mathrm{Ra}_{L_c} < 3\times10^{10} \end{aligned} \tag{6.18}$$

Alternatively, for the heated plate which is facing down or the cooled plate that is facing up we instead have:

$$\begin{aligned} &\mathrm{Nu}_{L_c} = 0.27\mathrm{Ra}_{L_c}^{1/4}, \qquad 3\times10^5 < \mathrm{Ra}_{L_c} < 3\times10^{10} \\ &\left[\begin{array}{l} \text{properties, except } \beta, \text{ at } t_m \\ \beta, \text{ at } t_m \text{ for liquids, } t_f \text{ for gases} \end{array}\right] \end{aligned} \tag{6.19}$$

6.8 Conclusion

First the material properties of interest in heat convection are defined. What follows is the explanation of the boundary layer concept and the cause of laminar and turbulent flow during the process of convection. Then Newton's cooling law is introduced and applied to derive the governing functions for natural convection. At the end, a detailed process is presented for the calculation of the heat transfer coefficient.

Chapter 7 Thermal Radiation

7.1 Introduction

The foregoing discussion of mechanisms of conduction and convection has shown that in both cases some physical medium is necessary for the transmission of the energy from the high temperature source to the low temperature sink. Generally speaking, the rate of flow of the thermal energy in these cases is proportional to the difference in temperature between the source and the sink. However, if a heated body is physically isolated from its cooler surroundings (i.e., by a vacuum), its temperature still tends to decrease in time, again showing a loss of energy. In this case an entirely different energy transfer mechanism is taking place, and it is called thermal radiation.

Thermal radiation is one aspect of radiant energy. Usually when radiant energy is incident on a body and is absorbed, it may turn into a form of thermal internal energy, a chemical reaction, etc., depending on the nature of the incident energy and the composition of the body. In this chapter only thermal radiation, i.e., radiant energy produced by thermal excitation of a body will be dealt with.

Two theories have been dominant in explaining the mechanism of energy radiation. One holds that a body emits discrete packets, or quanta, of energy and this theory has been successful in explaining the experimental facts observed in thermal radiation emission. Another theory asserts that radiation may be represented as an electromagnetic wave motion and has been useful in explaining such phenomena as interference of light, etc. At the present time a dual theory is generally accepted, giving radiant energy the characteristics of a wave motion as well as discontinuous emission.

7.2 Definition of Interest in Thermal Radiation

7.2.1 Emissive power

- The term emissive power is used to denote the emitted thermal radiation leaving a surface, per unit time, per unit area of surface.
- The total hemispherical emissive power of a surface is all the emitted energy, summed over all directions and all wavelengths, and is usually denoted by the symbol E. The total emissive power is found to be dependent upon the temperature of the emitting surface, the substance of which the surface is composed, and the nature of the surface structure (i.e., roughness, etc.).
- The monochromatic emissive power, symbolized by E_λ, is then defined as the rate, per unit of area, at which a surface emits thermal radiation at a particular wavelength, λ. Thus, the total and monochromatic hemispherical emissive powers are related by

$$E = \int_0^\infty E_\lambda d\lambda \tag{7.1}$$

and the functional dependence of E_λ on λ must be known to evaluate E.

It should be noted that the emissive power, total or monochromatic, consists only of the original emission leaving a surface. It does not include any energy leaving a surface that is the result of the reflection of any incident radiation.

7.2.2 Absorptivity, Reflectivity, and Transmissivity

When radiation energy is incident on a surface, part of it may be reflected away from the surface, part of it may be absorbed by the surface, and part of it may be transmitted through the surface. These fractions of reflected, absorbed, and transmitted energy are interpreted as surface properties called reflectivity, absorptivity and transmissivity, respectively. Here only the surface behavior with respect to incident energy summed over all wavelengths is worth concern. The following symbols are used:

$$\begin{aligned} \rho &= \text{total reflectivity=fraction reflected at all wavelengths} \\ \alpha &= \text{total absorptivity=fraction absorbed at all wavelengths} \\ \tau &= \text{total transmittivity=fraction transmitted at all wavelengths} \end{aligned} \tag{7.2}$$

Using the above definitions, energy conservation gives

$$\rho + \alpha + \tau = 1 \tag{7.3}$$

These surface properties usually depend on the surface composition and its temperature. In the case of gases, these properties are also dependent on the geometrical size and shape of the gas through which the radiation passes. Most gases have higher values of τ and low values of α and ρ. For instance, air at atmospheric pressure is virtually transparent to thermal radiation, so that one may take $\alpha \approx \rho \approx 0$ and $\tau \approx 1$. However, most solids

encountered in engineering practice are opaque to thermal radiation, so that $\alpha + \rho = 1$ and $\tau \approx 0$.

7.3 Blackbody Radiation

A perfect blackbody is defined as one which absorbs all incident radiant power regardless of the spectral distribution or directional character of the incident radiation, i.e., $\alpha = 1$ or $\rho = 0$. The emissive power of a blackbody, denoted by E_b, is dependent on the surface temperature only.

7.3.1 The Stefan-Boltzman Law for Blackbody Emissive Power

Based on experiments, Josef Stefan in 1879 suggested that the total emissive power of a blackbody is proportional to the fourth power of the absolute temperature. Later, Ludwig Boltzman applied the principles of classical thermodynamics and analytically derived the same fact. Thus the following dependence of E_b on T is called the Stefan-Boltzman law:

$$E_b = \sigma_{SB} T^4 \tag{7.4}$$

in which σ_{SB} is the Stefan-Boltzman constant with the value

$$\sigma_{SB} = 5.670 \times 10^{-8}\ \mathrm{W/m^2 \cdot {}^{\circ}K^4} \tag{7.5}$$

The temperature of the black surface is the absolute temperature.

The Stefan-Boltzman law for the total emissive power gives the total energy emitted by a blackbody, summed over all wavelengths.

7.4 Radiation of Nonblack Surfaces

A nonblack surface exhibits absorptivity less than unity, and its value may be dependent on the wavelength of the incident radiation. The hemispherical total emissivity is defined as the ratio of the total emissive power of a nonblack surface to that of a blackbody at the same temperature:

$$\varepsilon(T) = \frac{E(T)}{E_b(T)} \tag{7.6}$$

Therefore, the emissive power of a nonblack surface is readily calculated when ε is known:

$$E(T) = \varepsilon\alpha T^4 \tag{7.7}$$

7.4.1 Kirchhoff's Law

Kirchhoff's Law in the total sense

$$\alpha(T) = \varepsilon(T) \tag{7.8}$$

occurs when either of the two following conditions is met:

- if the incident irradiation on the receiving surface has a spectral distribution identical to that of the emission from a blackbody at the same temperature.
- if the receiving surface is an ideal gray surface, i.e., ε_λ is not a function of λ so that it may be moved from under the integral signs when deducing the total form of Kirchhoff's law with the use of the monochromatic form.

7.5 Shape Factor for Radiation Exchange

Of basic importance is the direct exchange of energy between two surfaces—that fraction of the energy leaving one surface that strikes the second directly; energy transferred indirectly by reflection or re-radiation from other surfaces is not included. This direct flux between one surface and another is expressed in terms of the shape factor, which is found by determining the exchange between different area elements in each surface and then performing simultaneous integrations over both surfaces.

7.5.1 Calculation of Shape Factor

The geometry of the problem is illustrated in Fig. 7.1. Two surfaces denoted by A_1 and A_2, respectively, are located arbitrarily in space with arbitrary shapes. They are not necessarily planes. Elements of each surface are denoted by dA_1 and dA_2 with corresponding normals N_1 and N_2. The line connecting dA_1 and dA_2 has length r and makes polar angles θ_1 and θ_2 with the two normals N_1 and N_2, respectively. The fraction of the flux leaving dA_1 which is intercepted by dA_2 is

$$df = I_1 \cos\theta_1 d\omega_{2-1} \tag{7.9}$$

where I_1 represents the intensity of the radiation leaving dA_1 and $d\omega_{2-1}$ is the solid angle subtended by dA_2 at dA_1. Projecting dA_2 normal to the radial line r gives $d\omega_{2-1} = (dA_2 \cos\theta_2)/r^2$, so that

$$df = I_1 \frac{\cos\theta_1 \cos\theta_2}{r^2} dA_2 \tag{7.10}$$

Since df is the portion of the flux from dA_1 intercepted by dA_2, it may be written as

$$df = \frac{dq_{1\to 2}}{dA_1} = I_1 \frac{\cos\theta_1 \cos\theta_2}{r^2} dA_2 \tag{7.11}$$

where $q_{1\to 2}$ represents the energy leaving all of A_1 that strikes all of A_2. Thus, $q_{1\to 2}$ is found by integrating the above expression over both areas:

$$q_{1\to 2} = \int_{A_1}\int_{A_2} I_1 \frac{\cos\theta_1 \cos\theta_2}{r^2} dA_2 dA_1 \tag{7.12}$$

If the radiosity of the originating surface, J_1, is uniform over that surface, the total energy leaving it is $A_1 J_1$, so the fraction of the energy leaving A_1 which strikes A_2 is

$$F_{1-2} = \frac{q_{1\to 2}}{A_1 J_1} \tag{7.13}$$

If, in addition, the radiant energy leaving A_1 is diffuse (both the emissive and reflected portions), then I_1 is a constant and $J_1 = \pi I_1$. Thus, the two equations above give

$$F_{1-2} = \frac{1}{A_1}\int_{A_1}\int_{A_2} \frac{\cos\theta_1 \cos\theta_2}{\pi r^2} dA_2 dA_1 \tag{7.14}$$

The factor F_{1-2} is called the shape factor of A_1 with respect to A_2—the fraction of the energy leaving A_1 which directly strikes A_2. As may be seen from its representation in (7.14), the shape factor for diffuse radiation is a purely geometric property of the two surfaces involved. The order of the subscripts on F_{1-2} is quite important since F_{2-1} will

be used to represent the fraction of energy leaving A_2 which directly strikes A_1. In general, $F_{1-2} \neq F_{2-1}$, since similar analysis yields

$$F_{2-1} = \frac{1}{A_2} \int_{A_2} \int_{A_1} \frac{\cos\theta_1 \cos\theta_2}{\pi r^2} dA_1 dA_2 \tag{7.15}$$

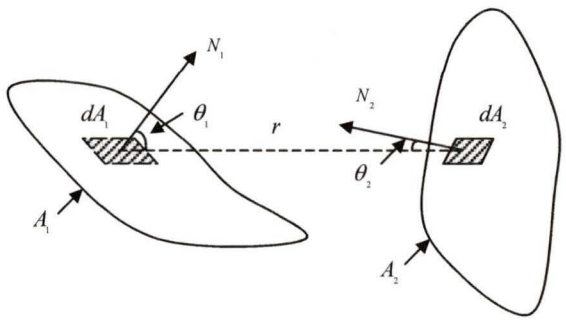

Figure. 7.1 Shape factor between two arbitrarily shaped and located surfaces

7.5.2 Properties of the Shape Factor

- The reciprocal property

For two surfaces, A_1 and A_2, in general $F_{1-2} \neq F_{2-1}$; however, the following reciprocal relation exists:

$$A_1 F_{1-2} = A_2 F_{2-1} \tag{7.16}$$

- The additive property

If one of the two surfaces, say A_i, is divided into sub-areas $A_{i_1}, A_{i_2}, \Lambda, A_{i_n}$ (so that $\sum A_{i_n} = A_i$), the following relation exists:

$$A_i F_{i-j} = \sum_n A_{i_n} F_{i_n - j} \tag{7.17}$$

The reciprocal relation given above then yields

$$F_{j-i} = \sum_n F_{j-i_n} \tag{7.18}$$

Thus, if the transmitting surface is subdivided, the shape factor for that surface with respect to a receiving surface is not simply the sum of the individual shape factors, although the AF product is expressed by such a sum. The shape factor from a surface to a subdivided receiving surface is simply the sum of the individual shape factors.

If surface A_i is subdivided into n parts ($A_{i_1}, A_{i_2}, \Lambda, A_{i_n}$) and surface A_j into m parts ($A_{j_1}, A_{j_2}, \Lambda, A_{j_m}$), the above reasoning leads to

$$A_i F_{i-j} = \sum_n \sum_m A_{i_n} F_{i_n - j_m} \tag{7.19}$$

These additive properties are useful in finding the shape factor for complex shapes by subdividing the surfaces into subsections for which the shape factor is either known or simply evaluated.

- The Enclosure Property

If the interior surface of a completely enclosed space is subdivided into n parts, each part having a finite area A_1, A_2, Λ, A_n, then

$$\sum_{j=1}^{n} F_{i-j} = 1, \qquad i = 1,2,\Lambda\ ,n \tag{7.20}$$

The above representation admits the shape factors $F_{1-1}, F_{2-2}, \Lambda\ , F_{n-n}$ since some of the surfaces may "see" themselves if they are convex. If a surface A_1 is completely enclosed by a second surface, A_2, and if A_1 does not see itself ($F_{1-1} = 0$) then $F_{1-2} = 1$, then we have

$$F_{2-1} = \frac{A_1}{A_2} \tag{7.21}$$

The above properties will be useful for the determination of shape factors for specific geometries and for the analysis of heat exchange between surfaces.

7.5.3 Shape Factor Between Two Arbitrary Sizes of Rectangular Planes

Since in most thermal applications in Microwave Engineering, calculation of the shape factor between two arbitrary sizes of rectangular planes is of essential importance, [18]Hsu has presented a method of integration for deriving such explicit equations for calculating the shape factor between two arbitrary sizes of rectangles (having sides parallel to each other) which are placed on mutually parallel planes.

The definition of the shape factor for radiative transfer between two finite areas, "1" and "i", is given by the following equation:

$$\overline{F}_{1-i} = \frac{1}{A} \int_{A_1} \int_{A_2} \frac{\cos\theta_1 \cos\theta_2}{\pi s'^2} dA_i dA_1 = \frac{1}{A_1} \int_{A_1} F_{1-i} dA_1 \tag{7.22}$$

The feasibility of computing the above integral depends largely upon the sizes and the relative position of the two areas. For rectangles of equal size that are placed in an opposite manner, evaluation of the integral is relatively straightforward. If the two rectangles are of different sizes and are placed in an arbitrary position such as shown in Fig. 7.2, then evaluation of the integral becomes much more complicated because of the difficulty in specifying the integration limits. The mathematical scheme for evaluating the integral for this latter case is discussed as follows.

First, choose F_{1-i} such that a normal through one corner of A_1 passes through dA_1. Referring to Figure. 7.3 a, then, the shape factor between the two rectangles A_1 and A_2, can be written as:

$$F_{1-2} = \frac{1}{A_1} \int_{A_1} \left\{ F_{1-(2+\alpha+\beta+\gamma)} - F_{1-(\alpha+\gamma)} - F_{1-(\beta+\gamma)} + F_{1-\gamma} \right\} dA_1 \tag{7.23}$$

Also, the coordinate variables are found to be as follows:

F_{1-i}	$x-$coordinate	$y-$coordinate	sign
$F_{1-(2+\alpha+\beta+\gamma)}$	$l+x$	$c+m-y$	+
$F_{1-(\alpha+\gamma)}$	$l+x$	$m-y$	−
$F_{1-(\beta+\gamma)}$	$l+x-d$	$c+m-y$	−
$F_{1-\gamma}$	$l+x-d$	$m-y$	+

(7.24)

Accordingly, the expression of the integrals in (7.23) is, for example:

$$\frac{1}{A_1}\int_{A_1} F_{1-(\alpha+\beta+\gamma)}\,dA_1$$

$$= \frac{1}{2\pi ab}\left\{\begin{array}{l} \int_0^a\int_0^b \dfrac{c+m-y}{\sqrt{(c+m-y)^2+h^2}}\tan^{-1}\dfrac{l+x}{\sqrt{(c+m-y)^2+h^2}}\,dxdy \\ +\int_0^a\int_0^b \dfrac{l+x}{\sqrt{(l+x)^2+h^2}}\tan^{-1}\dfrac{c+m-y}{\sqrt{(l+x)^2+h^2}}\,dxdy \end{array}\right\} \qquad (7.25)$$

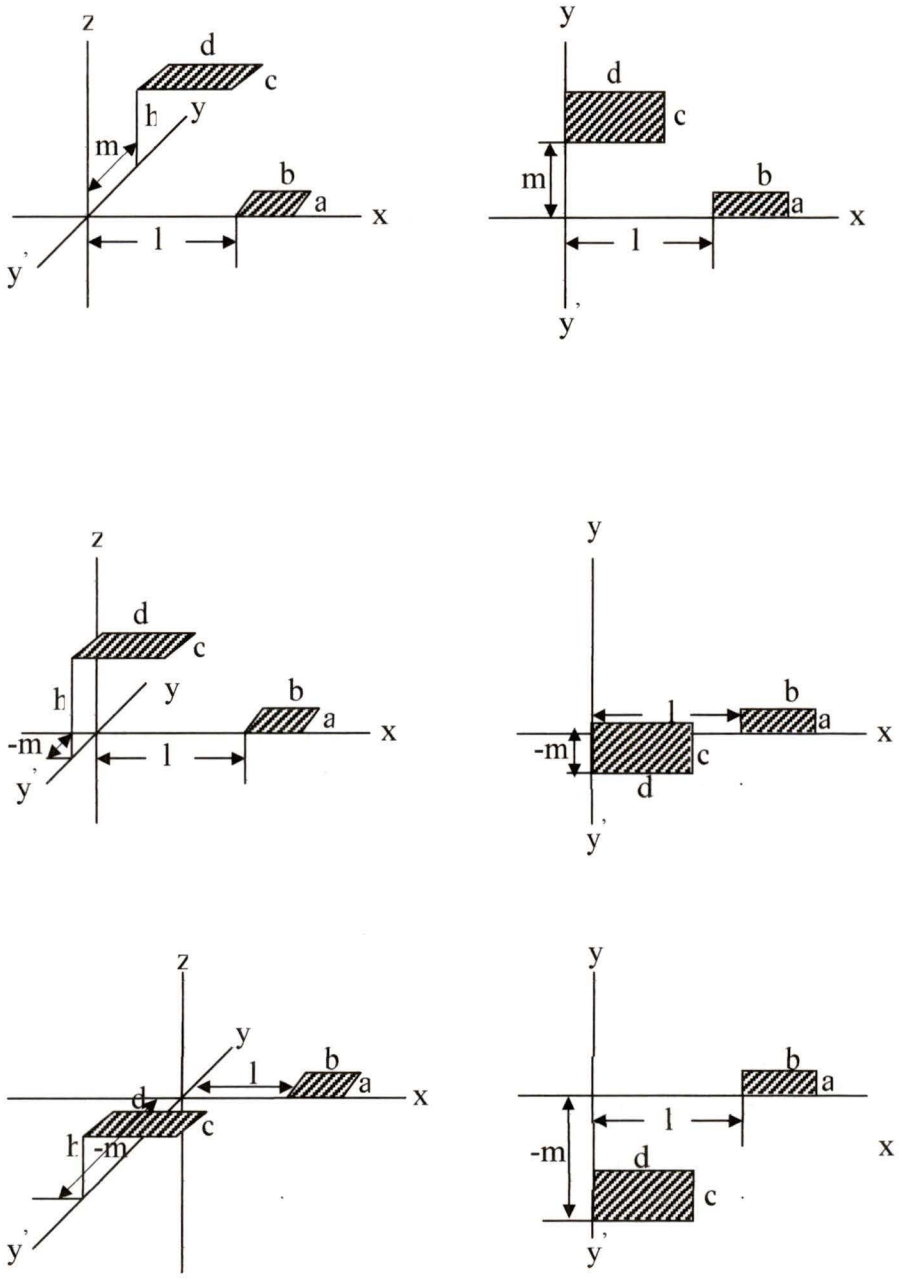

Figure. 7.2 Two rectangles of different sizes and placed in an arbitrary position

It should be pointed out that Eq. (7.23) is applicable only when the conditions $l > d$ and $m > a$ are simultaneously satisfied. For other cases, such as the one shown in Figure. 7.3 b, it is necessary to modify the expressions for the F_{1-i}'s in Eq. (7.23), since F_{1-2} does not remain identical for all the differential elements taken inside A_1. In Figure. 7.3 b, for instance, although the expression for F_{1-2} remains the same as that in Eq. (7.23) for an area element at point "P", it should be changed to

$$F_{1-2} = F_{1-\alpha'} + F_{1-\beta'} + F_{1-\gamma'} + F_{1-\delta'} \tag{7.26}$$

At first glance then, evaluation of $\overline{F}_{1-2}$ may appear extremely cumbersome since the area A_1 must be subdivided into sections and evaluation of the integrals carried out for each section. Fortunately, however, close examination of the coordinate variables in Eq.(7.24) reveals that they will automatically adjust their signs such that the expression for F_{1-2} remains valid for all the area elements taken inside A_1. For example, the coordinate variables for F_{1-2} at point "Q" can be found to be equivalent to those at point "P" as shown below

F_{1-i}	$x-$coordinate	$y-$coordinate	sign	equivalent to
$F_{1-\alpha'}$	$l+x$	$c+m-y$	+	$F_{1-(2+\alpha+\beta+\gamma)}$
$F_{1-\beta'}$	$l+x$	$y-m=-(m-y)$	+	$-F_{1-(\alpha+\gamma)}$
$F_{1-\gamma'}$	$d-l-x=-(l+x-d)$	$c+m-y$	+	$-F_{1-(\beta+\gamma)}$
$F_{1-\delta'}$	$d-l-x=-(l+x-d)$	$y-m=-(m-y)$	+	$F_{1-\gamma}$

(7.27)

This coincidence is partially due to the symmetrical form of F_{1-i} and to the fact that $\tan^{-1}(-\psi) = -\tan^{-1}\psi$. It can further be shown that, for $l \geq 0$, Eq. (7.23) is also valid for

the cases shown in Figure. 7.2 b and Figure. 7.2 c, for which the sign of "m" in Eq. (7.24) becomes negative, in order to obtain satisfactory results.

The equation in Appendix A-1, although formidable in appearance, can be simplified considerably for several special cases. For instance, by letting $L = M = 0$, $C = A$ and $B = D$, the equation reduces to the equation for two parallel rectangular planes of equal size which are located opposite to each other. By letting $M = 0$, $C = A$, $B = D$, $L = 1/h = \cos\theta$, one obtains the shape factor equation for the case where two rectangles of equal size are placed obliquely on parallel planes.

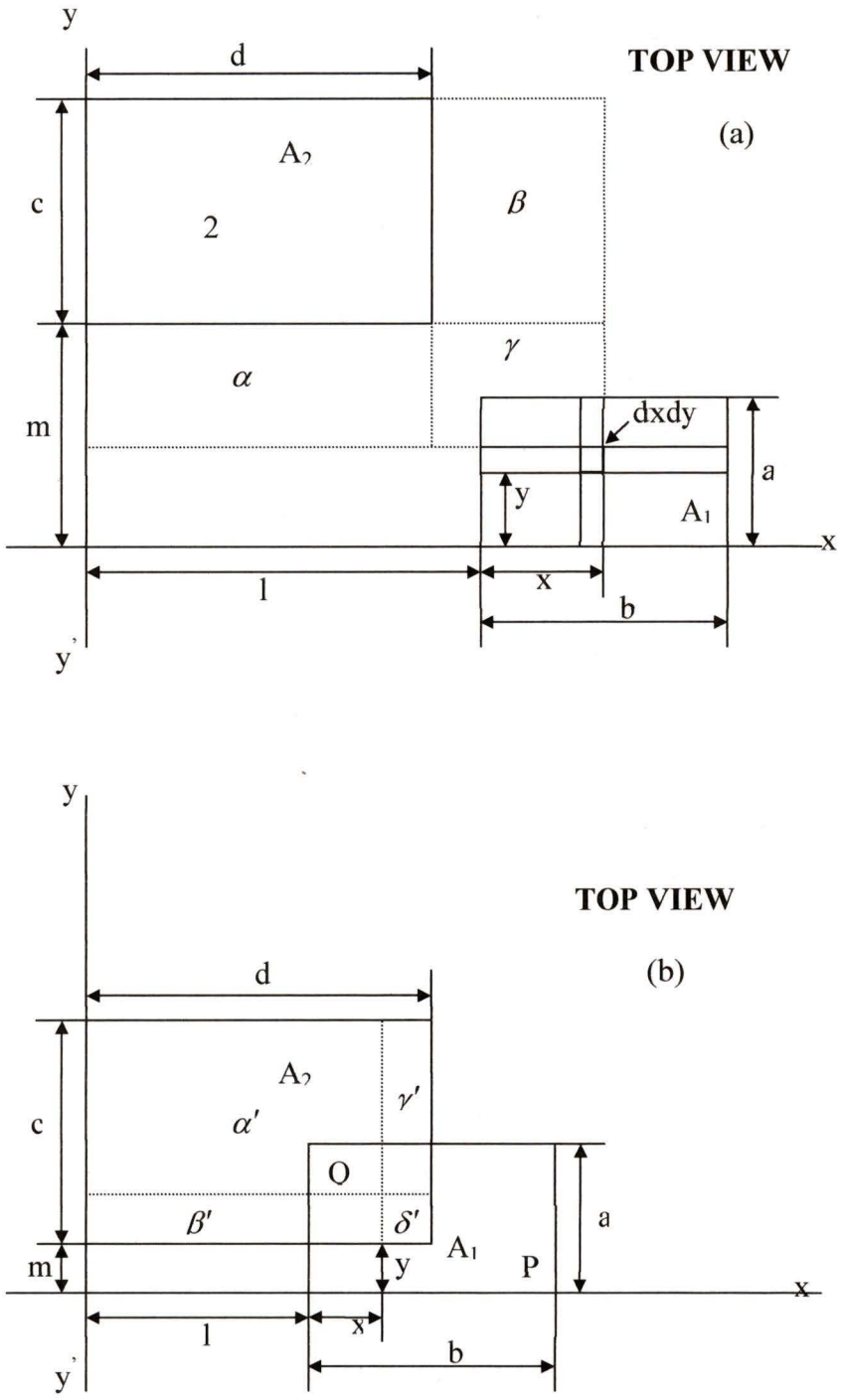

Figure. 7.3 Top view of two rectangles of different sizes and placed in an arbitrary position

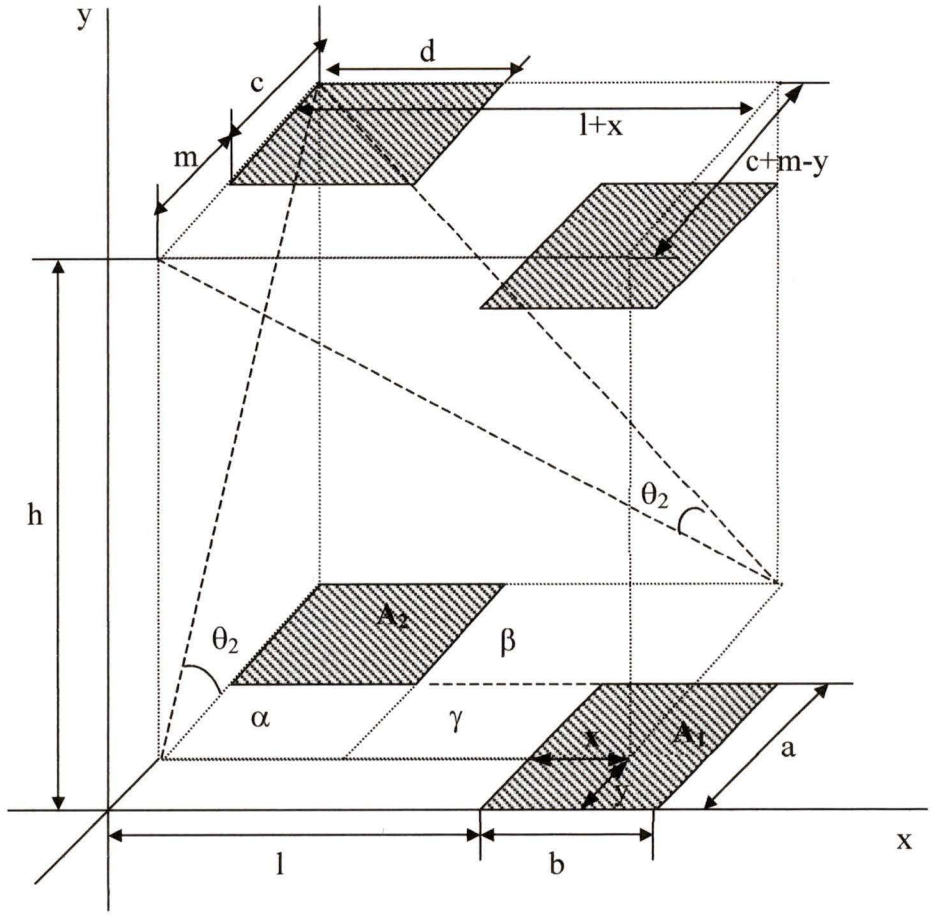

Figure. 7.4 3D illustration of the lengths and angles used in above equations

7.6 Lumped Thermal Capacity Model for Combined Convection and Radiation

The heat transfer coefficient is usually assumed constant during the cooling period for forced convection. This assumption is less appropriate for natural convection especially when thermal radiation is significant. The natural convection heat transfer coefficient $\overline{h}_c$

is proportional to $\Delta T^{1/4}$ for laminar flow and to $\Delta T^{1/3}$ for turbulent flow. The temperature difference $\Delta T = T - T_f$ decreases as the body cools, as does $\bar{h}_c$. Radiation heat transfer is proportional to $\left(T^4 - T_f^4\right)$. In order to apply Newton's law of cooling for the situation where both convection and radiation are important, a lumped thermal capacity analysis is extended to allow for a variable convective heat transfer coefficient.

7.6.1 Governing Equation and Initial Condition

Fig. 7.5 shows a body that loses heat by both convection and radiation. For a small gray body in large, nearly black surroundings also at temperature T_f, the radiation heat transfer is obtained as $Q = \varepsilon A\sigma\left(T^4 - T_f^4\right)$.

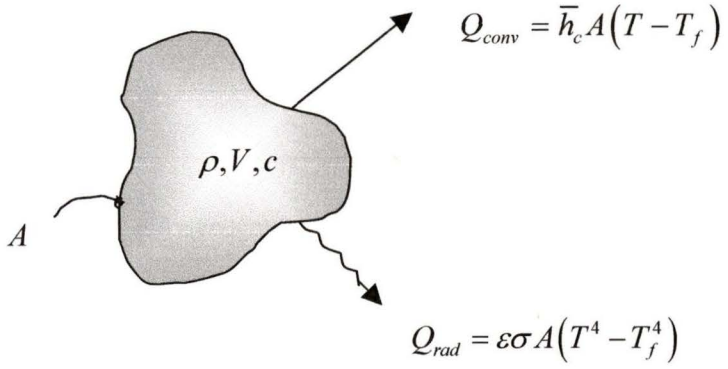

Figure. 7.5 Schematic of a body losing heat by convection and radiation for a lumped thermal capacity model

The energy conservation principle yields:

$$\rho Vc\frac{dT}{dt} = -\bar{h}_c A\left(T - T_f\right) - \varepsilon A\sigma\left(T^4 - T_f^4\right) \tag{7.28}$$

or

$$\frac{dT}{dt} = -\frac{\bar{h}_c A}{\rho Vc}\left(T - T_f\right) - \frac{\varepsilon A\sigma}{\rho Vc}\left(T^4 - T_f^4\right) \tag{7.29}$$

where

$$\begin{aligned} &\rho \text{ is the density of body} \\ &V \text{ is the volume of body} \\ &c \text{ is the specific heat of body} \end{aligned} \tag{7.30}$$

The initial condition is again

$$t = 0; \qquad T = T_0 \tag{7.31}$$

This first-order ordinary differential equation has no closed-form analytical solution even when the convective heat transfer coefficient $\bar{h}_c$ is constant as in forced convection. However, Eq. (7.29) can be solved easily using a numerical integration procedure. For this purpose, it can be rearranged as

$$\frac{dT}{dt} + \frac{hA}{\rho Vc}\left(T - T_f\right) = 0 \tag{7.32}$$

$$h = \bar{h}_c + h_r = B\left(T - T_f^{\,n}\right) + \sigma\varepsilon\left(T^2 + T_f^2\right)\left(T + T_f\right) \tag{7.33}$$

where $\left(T^4 - T_f^4\right)$ has been factored, as was done in deriving Eq. (7.29). For forced convection, $n = 0, B = \bar{h}_c$; for laminar natural convection $n = 1/4$ and B is a constant [for example, for a plate of height L, $B = (4/3)(1.07)/L^{1/4}$]. Eq. (7.33) defines a total heat transfer coefficient that accounts for both convection and radiation and changes continuously as the body cools. To put Eq. (7.33) in dimensionless form, we use the dimensionless variables:

$$T^* = \frac{T - T_f}{T_0 - T_f}, \qquad t^* = \frac{t}{t_c} \tag{7.34}$$

The definition of the time constant t_c poses a problem since h is not a constant as before. We choose to define t_c in terms of the value h at time $t = 0$, when the body temperature is T_0:

$$t_c = \frac{\rho V c}{h_0 A} = \frac{\rho V c}{\left[B\left(T_0 - T_f\right)^n + \sigma\varepsilon\left(T_0^2 + T_f^2\right)\left(T_0 + T_f\right)\right]A} \tag{7.35}$$

Eq. (7.33) then becomes

$$\frac{dT^*}{dt} + \frac{h}{h_0}T^* = 0 \tag{7.36}$$

with the initial condition

$$t^* = 0: \qquad T^* = 1 \tag{7.37}$$

Numerical integration is possible for this problem.

7.7 **Conclusion**

First the material property of interest in heat radiation is defined. Then discussion on the mechanism of blackbody and nonblack body thermal emissive power is carried out. A great deal of effort is put into the calculation of shape factors in order to determine the power exchange between two mutually visible surfaces. Finally a lumped thermal capacity model is formulated for combined convection and radiation.

Chapter 8 Numerical Analysis and Simulation Results

8.1 Numerical Analysis

Formulas listed in this section are all derived from the theorem and algorithm introduced in Part II " Coupled TLM-Thermal Analysis" in this thesis. This section is to deliberately and comprehensively get those essential formulas together in order to make it easy for the readers to obtain the idea of TLM-Thermal Coupling process.

8.1.1 Comprehensive Formulation

- Power absorbed by imperfect conductors and dielectrics

According to Poynting's theorem, the time-average power dissipated in the volume V due to conductivity, dielectric, and magnetic losses is defined as:

$$P_{EM} = \frac{\sigma}{2}\int_V \left|\overline{E}\right|^2 dv + \frac{\omega}{2}\int_V (\varepsilon''\left|\overline{E}\right|^2 + \mu''\left|\overline{H}\right|^2)dv \tag{8.1}$$

Where σ is the electric conductivity, ω is angular frequency, $\overline{E}, \overline{H}$ are the total electric and magnetic fields in the volume V and ε'', μ'' are the imaginary parts of the complex permittivity and permeability.

The calculation of the power absorbed by a good conductor can be simplified by determining the tangential magnetic field at the surface of the conductor:

$$P_{EM} = \frac{R_s}{2} \int_{S_0} \left|\overline{H}\right|^2 ds \tag{8.2}$$

Where $\overline{H}$ is the tangential magnetic field at the conductor surface S_0 and

$$R_s = \mathrm{Re}(\eta) = \sqrt{\frac{\omega\mu}{2\sigma}} \tag{8.3}$$

is called the surface resistivity of the conductor.

The average electromagnetic power dissipation P_{EM} is first calculated using a GSCN 3D TLM algorithm. It is then used as the power distribution input for the thermal analysis. Three mechanisms of heat transfer are investigated: conduction, convection and radiation with the following assumptions:

1) No forced cooling mechanism is present, thus only free convection is considered.
2) The outer surfaces of the vertical waveguide walls are assumed smooth so that the airflow along these walls is laminar.
3) Convection inside the waveguide is negligible due to the small dimensions of the waveguide.

- Heat Conduction

Heat conduction is modeled with a finite difference scheme assuming the temperature inside a FDTD cell to be homogeneous. A uniform mesh is used for the calculation of conduction heat flux. The heat conduction is computed in such a way that for every single cell the power flux in all the six directions is computed individually and then summed up to yield the total heat power flux through that cell.

The power flux in positive X direction is:

$$PXP_{i,j,k} = \frac{2\Delta l k_{i,j,k} k_{i+1.j,k}}{k_{i,j,k} + k_{i+1.j,k}} (T_{i,j,k} - T_{i+1,j,k}) \tag{8.4}$$

The power flux in negative X direction is:

$$PXN_{i,j,k} = \frac{2\Delta l k_{i-1,j,k} k_{i,j,k}}{k_{i-1,j,k} + k_{i,j,k}} (T_{i-1,j,k} - T_{i,j,k}) \tag{8.5}$$

The power flux in positive Y direction is:

$$PYP_{i,j,k} = \frac{2\Delta l k_{i,j,k} k_{i,j+1,k}}{k_{i,j,k} + k_{i,j+1,k}} (T_{i,j,k} - T_{i,j+1,k}) \tag{8.6}$$

The power flux in negative Y direction is:

$$PYN_{i,j,k} = \frac{2\Delta l k_{i,j-1,k} k_{i,j,k}}{k_{i,j-1,k} + k_{i,j,k}} (T_{i,j-1,k} - T_{i,j,k}) \tag{8.7}$$

The power flux in positive Z direction is:

$$PZP_{i,j,k} = \frac{2\Delta l k_{i,j,k} k_{i,j,k+1}}{k_{i,j,k} + k_{i,j,k+1}} (T_{i,j,k} - T_{i,j,k+1}) \tag{8.8}$$

The power flux in negative Z direction is:

$$PZN_{i,j,k} = \frac{2\Delta l k_{i,j,k-1} k_{i,j,k}}{k_{i,j,k-1} + k_{i,j,k}} (T_{i,j,k-1} - T_{i,j,k}) \tag{8.9}$$

Where k denotes the temperature-dependent thermal conductivity of the materials, and Δl is the cell size.

The total heat conduction power flux $P_{i,j,k}^{COND}$ is then obtained as

$$P_{i,j,k}^{COND} = PXN_{i,j,k} - PXP_{i,j,k} + PYN_{i,j,k} - PYP_{i,j,k} + PZN_{i,j,k} - PZP_{i,j,k} \tag{8.10}$$

- Heat Convection

Calculation of heat convection requires the knowledge of the heat transfer coefficient h defined as follows:

$$h = \frac{N_u k_{fluid}}{l} \tag{8.11}$$

N_u is the dimensionless heat transfer coefficient, k_{fluid} the thermal conductivity of the fluid, and l is the characteristic length of the surface that is usually obtained by dividing the surface area by the perimeter in the case of horizontal surfaces, or simply the height of the surface for vertical surfaces. Finally, the heat convection power flux is calculated as

$$P_{i,j,k}^{CVEC} = h_{i,j,k}(T_{i,j,k} - T_{fluid}) \tag{8.12}$$

- Heat Radiation

1) Calculation of free heat radiation from the outer boundaries of the structure

The emissive power of a "graybody" is a function of temperature and emissivity. The power flux is calculated as:

$$P_{i,j,k}^{FREERAD} = \varepsilon \sigma_{sB} {T_{i,j,k}}^4 \Delta l^2 \tag{8.13}$$

Where ε is the emissivity of the surface and σ_{SB} is Stefan-Boltzman constant.

2) Calculation of heat radiation exchange between the inner surfaces of the structure

Assuming that the inner surfaces are subdivided into discrete cells, the exchange of power between two cell surfaces (i, j, k) and (l, m, n) through radiation is

$$P_{rad} = \Phi_{(i,j,k)(l,m,n)} - \Phi_{(l,m,n)(i,j,k)} \tag{8.14}$$

where

$$\Phi_{(i,j,k)(l,m,n)} = \varepsilon_{i,j,k} \alpha_{l,m,n} F_{i,j,k,l,m,n} \sigma_{SB} T_{i,j,k}^4 \tag{8.15}$$

$$\Phi_{(l,m,n)(i,j,k)} = \varepsilon_{l,m,n} \alpha_{i,j,ki} F_{l,m,n,i,j,k} \sigma_{SB} T_{l,m,n}^4 \tag{8.16}$$

Here α is the absorptivity of the surface, which is usually equal to the emissivity of that surface, and F is the shape factor determined by geometry only. This coefficient is

defined as the part of energy transmitted from one cell surface s to another cell surface s', divided by the total energy emitted by the surface s.

$$F_{ss'} = \frac{1}{\pi A_s} \int_{A_s} \int_{A_{s'}} \frac{\cos(\theta_s)\cos(\theta_{s'})}{r^2} dA_s dA_{s'} \tag{8.17}$$

θ and r describe the relative positions of the surfaces s and s'. For details, refer to the chapter of "Thermal Radiation".

The exchange radiation power flux is then calculated as the sum of the heat exchanges between the specific cell and all the visible surface cells.

$$P_{i,j,k}^{EXRAD} = \sum_{\substack{Visible \\ Surfaces}} P_{rad} \tag{8.18}$$

- Updating Temperature

Once all the power fluxes are calculated, the temperature can be updated as follows:

$$\begin{aligned} T_{i,j,k}^{n+1} &= T_{i,j,k}^{n} + \frac{\Delta t}{m_{i,j,k} c_{i,j,k}} P_{i,j,k}^{TOTAL} \\ &= T_{i,j,k}^{n} + \frac{\Delta t}{\Delta l^3 \rho_{i,j,k} c_{i,j,k}} (P_{i,j,k}^{EM} + P_{i,j,k}^{COND} - P_{i,j,k}^{CVEC} - P_{i,j,k}^{FREERAD} - P_{i,j,k}^{EXRAD}) \end{aligned} \tag{8.19}$$

where Δt is the thermal calculation time step, ρ is the density and c is the specific heat.

When the total power flux entering the structure equals to the total power flux emerging from it, the temperature reaches a steady state.

8.1.2 Flow Chart

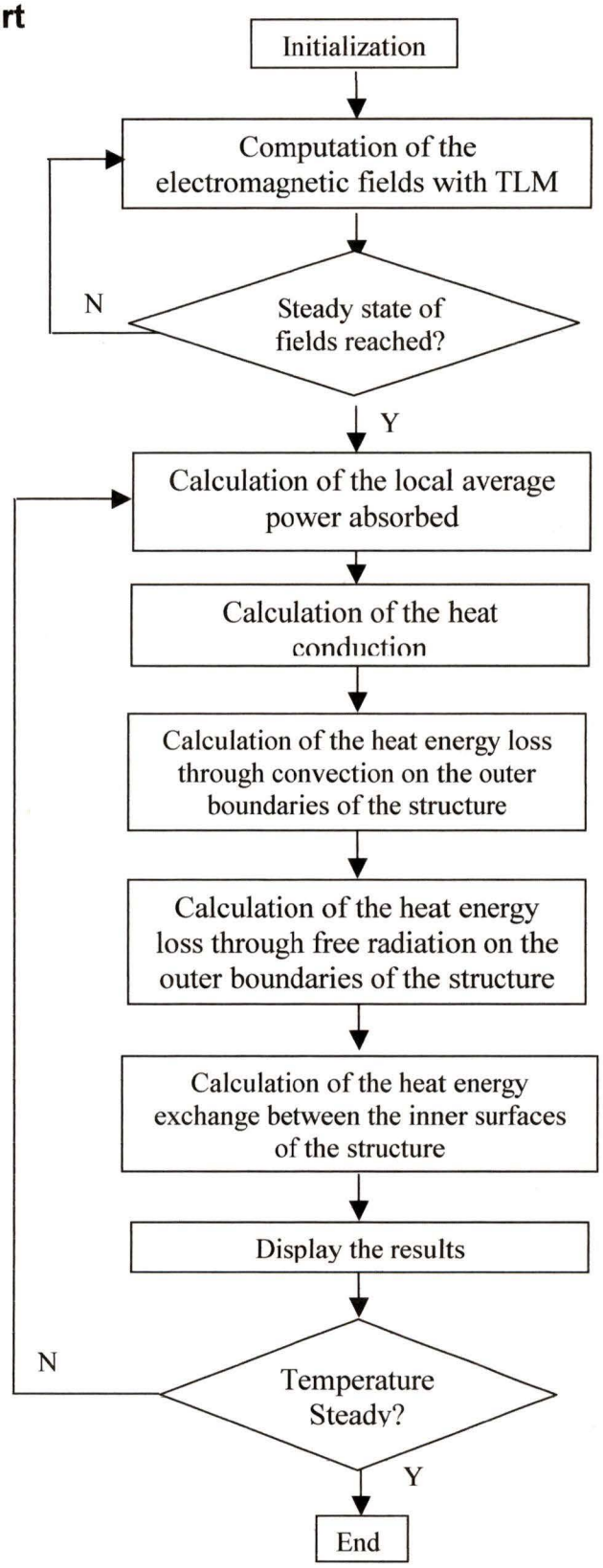

8.2 Simulations Results

The algorithm has been applied to analyze the thermal behavior of a microwave cavity with a polyvinyl chloride (PVC) sample placed inside. The permittivity for PVC is chosen to be 3.5 F/m and thermal conductivity for PVC is 0.146538W/m-K [30].

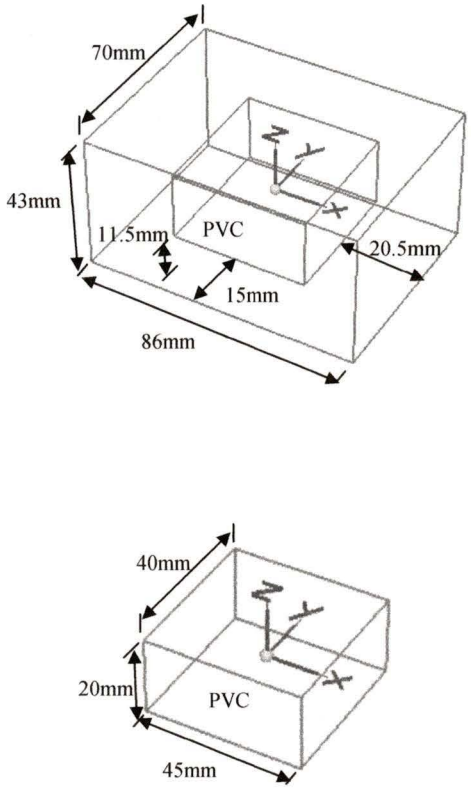

Figure. 8.1 Topology of the structure: a microwave cavity with a PVC sample placed inside

The structure is excited with the TE_{110} mode at 2.2GHz . The electromagnetic field heats the PVC sample approximately at a constant heating rate of 2W. Most microwave energy losses occur in the dielectric, dominating the losses in the metal surfaces. Furthermore,

the largest power absorption occurs in the middle of the PVC block due to the TE_{110} mode field distribution. As a result, the temperature in the middle of the PVC block increases at a faster rate than the other regions inside the structure.

Two sampling probes are placed inside the cavity, one in the air region and the other at the middle of the PVC block. The change in temperature over time at these probes is shown in Figure. 8.3 (b) and (c). The temperature distribution in Figure. 8.3 correlates with the TE110 mode field distribution.

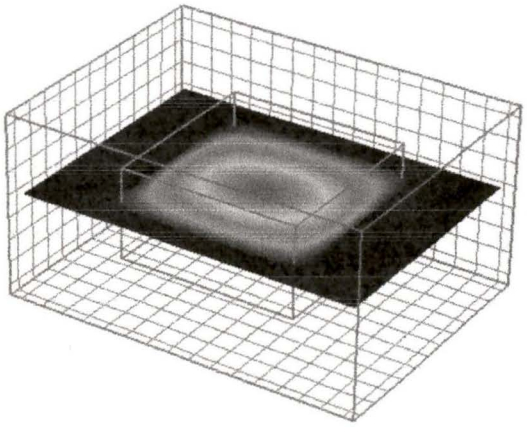

(a) 3D color representation

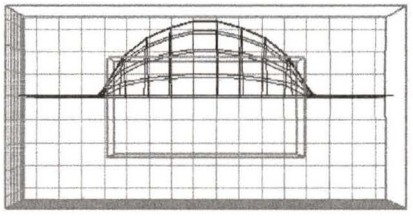

(b) 2D wire mesh representation

Figure. 8.2 TE_{110} mode power distribution in a PVC (ε_r=3.5, σ=2.e-6 S/m) loaded cavity. In the 3D color representation, red (center) and deep blue (background) colors are corresponding to 0.0156-W and 0-W, respectively. The 2D wire mesh representation gives the same information in another perspective.

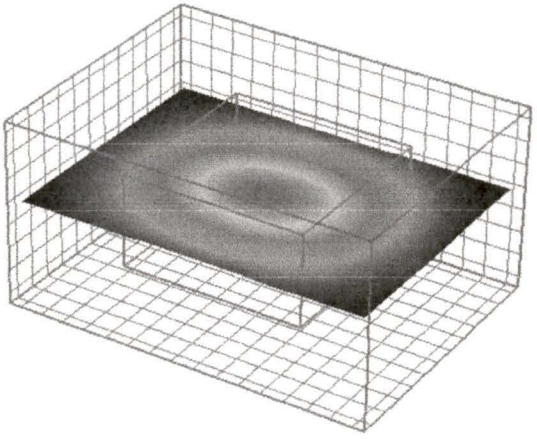

(a) 3D color representation

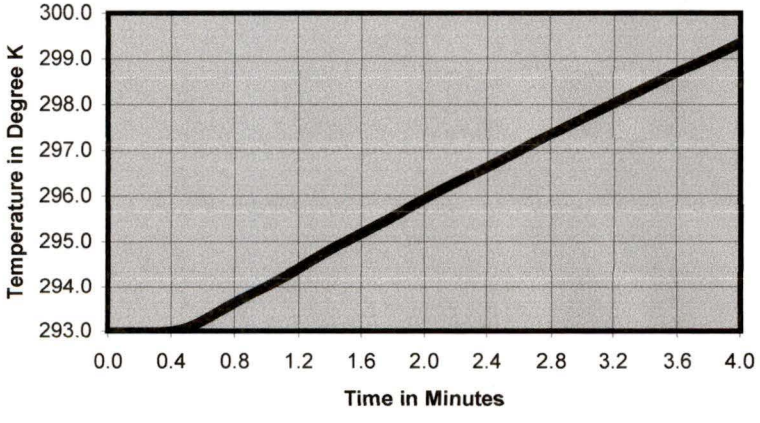

(b) Temperature increase in the center of the PVC block

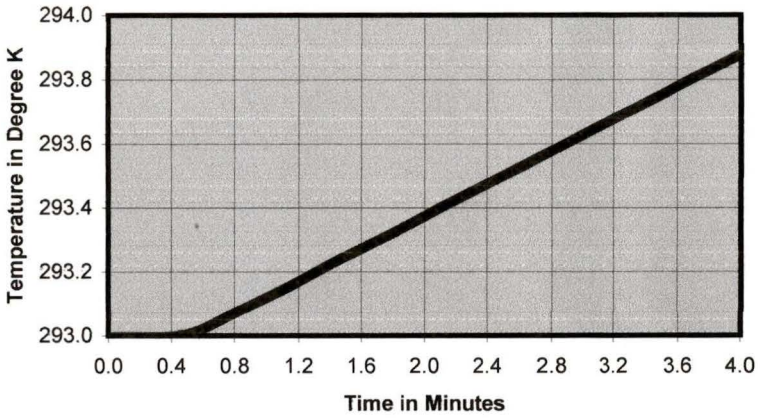

(c) Temperature increase in the air around the PVC block

Figure. 8.3 Temperature distribution in the PVC loaded cavity. (a) Red (center) and deep blue (background) color are corresponding to 299.3^{o}K and 293^{o}K, respectively. The temperature evolution in the PVC block and in the air are shown in (b) and (c). The total power dissipated in the PVC region is 2-W, which is equivalent to a 0.0345^{o}K/s heating rate. This value agrees well with the slope of the graph in Figure. 8.3 (b), which is 0.0325^{o}K/s.

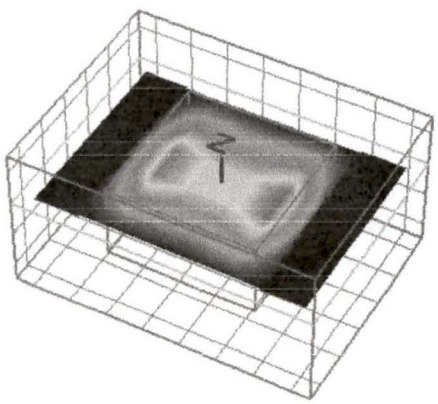

Figure. 8.4 Initial temperature distribution inside the computational domain with the excitation of TE210 mode field distribution

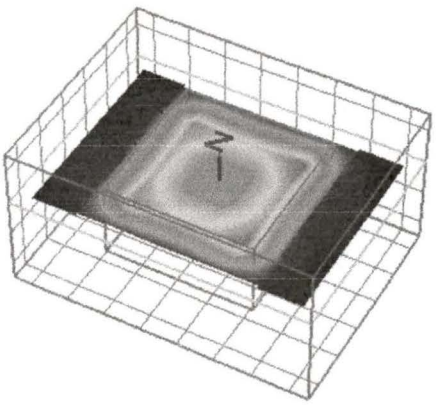

Figure. 8.5 Initial temperature distribution inside the computational domain with the excitation of TE220 mode field distribution

8.3 Error Analysis

- As has been pointed out previously, the numerical methods presented in this chapter represent approximate solutions to the original differential equations since derivatives are replaced by finite differences. Terms of the order of the fourth power of the spatial step size are neglected and, in the transient case, terms of the order of the square of the time increment are neglected. Thus, some degree of truncation error has been introduced by these approximations.
- Numerical errors may also be introduced into the solution if the mesh is too coarse or the time step is chosen to be too large.

Chapter 9 Conclusion

9.1 Conclusion

The object of this thesis is to seek new approach by the means of combining several numerical methods to the applications in which hybrid methods may give better performance.

The first attempt in the thesis is to derive a hybrid algorithm between MRTD and TLM methods. The idea is to simultaneously apply two different sets of grids to the structure of interest. The two methods are hybrid in such a way that MRTD is used to model subdomains of simple shape, while TLM is applied to analyze the complicated boundary geometry. Thus, the combination of two methods would be able to handle such a problem as the one with a large geometry and complex boundary if the stability problem could be solved successfully.

The second attempt is to develop a coupled EM-thermal engine so that it could be applied to solve the thermal problems in microwave engineering. For example, waveguide components usually contain discontinuities that give rise to reflection and storage of

energy. This storage of energy is always combined with wall losses that increase the temperature near the discontinuities. In fact, the temperature can become so high that the components be destroyed.

The thesis has presented a new approach to solve such problems. In the designed thermal engine, heat conduction is formulated using an explicit FDTD algorithm, with the temperature dependence of thermal conductivity taken into account. The conducting heat energy is not only propagating within one substance, but also transferred from one substance to another substance that has contact with it. Thermal convection in the application of microwave engineering is simplified with the assumption that no forced cooling system is present. Thus only microwave heated walls or dielectric objects cause the natural convection of fluid (usually air) immediately adjacent to it. Thermal radiation in free space is easily formulated with the empirical equations. However, the calculation of the shape factors between the surfaces inside the waveguide structure is the most crucial problem in the design of this thermal engine. The mutual visibility of two surfaces needs to be determined carefully and efficiently because otherwise the process of inner thermal heat exchange might be costly in time.

The designed thermal engine has been applied to analyze a microwave cavity with a PVC sample placed in the middle. Different source distributions have been tested and the temperature distribution corresponds to their source very well. However, due to the versatility of thermal situation, it is very hard to find in the literature some experimental data to reproduce and compare with. Thus, the quantitative accuracy needs further confirmation.

The thermal analysis tool is very useful in the thermal application of microwave engineering. It allows us to predict the temperature rise, the hot spot, the critical temperature point and optimize the power handling capability.

9.2 Future Research

A few features are to be implemented in the near future for the thermal engine.

One is the formulation of the thermal absorbing condition. The need for this arises from the existence of EM absorbing boundary. In case a waveguide structure has a relatively large dimension so that only a section of it needs to be modeled. A EM absorbing boundary will be put where the structure is cut short for simplicity of EM calculation. In such case, since there is no data about thermal properties at the location of the EM absorbing boundary, no practical thermal mechanism can represent the behavior there. Hence, an interpolation method needs to be applied to predict the temperature at the absorbing boundaries.

Another feature is the multiple coupling of EM and Thermal engine. That is, after a certain period, if the temperature rises more than a pre-set threshold so that the electrical properties of the substance within waveguide are affected, the EM process will reevaluate the affected properties and re-calculate the power dissipation, which is, the source distribution for thermal engine. Thereafter, the thermal process starts again, and so on, until the thermal process reaches equilibrium. In this way the coupling process is expected to give better representation of practical mechanism.

However, as to the coupling of TLM-MRTD, due to time limit, I would not be able to make any progress on this topic.

Bibliography:

[1] S.G. Mallat, "A Theory for Multiresolution Signal Decomposition: The Wavelet Representation", *IEEE Transactions on Pattern Analysis and Machine Intelligence*, 11(7):647-693, July 1989.

[2] I. Daubechies, "Orthogonal Bases of Compactly Supported Wavelets", *Communications on Pure and Applied Mathematics*, 41:909-996, 1988.

[3] M. Fujii, P. P. M. So, E. Hu, W. Liu and W. J. R. Hoefer, "A 2D TLM and Haar MRTD Real-Time Hybrid Connection Technique", *The 16th Annual Review of Progress in Applied Computational Electromagnetics*, pp. 1013-1020, March 20-24, 2000.

[4] M. Fujii, P. P. M. So, E. Hu, W. Liu and W. J. R. Hoefer, "Hybrid Connection between TLM and Haar MRTD Algorithms", *Proceedings of TLM Workshop*, Oct. 1999.

[5] G. Beylkin, R. Coifman, and V. Rokhin, "Fast Wavelet Transforms and Numerical Algorithms", *Communications on Pure and Applied Mathematics*, 64: 141-184, 1991.

[6] G. Kraser, *A friendly guide to wavelets,* Birkhauser, Boston, 1994.

[7] M. Werthen and I. Wolff, "A Novel Wavelet Based Time Domain Simulation Approach", *IEEE Microwave and Guided Wave Letters*, 6(12): 438-440, Dec. 1996.

[8] P. Russer, B. Bader, "The Alternating Transmission Line Matrix (ATLM) Scheme", *Proc. IEEE MTT-S International Microwave Symposium Digest,* 19-22, Orlando, Florida, May 16-20, 1995.

[9] W.J.R.Hoefer, P.P.M. So, *The Electromagnetic Wave Simulator Manual*, *John Wiley & Sons,* 1991.

[10] C. Eswarappa, W.J.R.Hoefer, "Bridging the Gap between TLM and FDTD", *IEEE Microwave and Guided Wave Letters,* Vol. 6, No. 1, pp. 4-6, January 1996.

[11] M. Krumpholz and L.P.B. Katehi. "New Prospects for Time Domain Analysis", *IEEE Microwave and Guide Wave Letters*, 5(11): 382-384, Nov. 1995.

[12] W. H. Press, S.A. Teukolsky, W.T. Vetterling, and B. P. Flannery, *Numerical Recipes in Fortran 77: The art of Scientific Computing*, 2nd ed., Cambridge University Press, Cambridge, 1992.

[13] Masafumi Fujii, "A Time-Domain Haar-Wavelet-Based Multiresolution technique for Electromagnetic Field Analysis", Ph.D Dissertation, Univ. of Victoria, 1999.

[14] D. M. Pozar, *Microwave Engineering,* 2nd Edition, John Wiley & Sons, Inc., New York, 1998.

[15] J. Haala, W. Wiesbeck, "Modeling Microwave and Hybrid Heating using FDTD", *The 16th Annual Review of Progress in Applied Computational Electromagnetics*, vol. 2, March 20-24, 2000.

[16] C. Viennet, P. P. M. So, W. J. R. Hoefer, "Modeling of Transient Thermal Behavior of Discontinuities in Rectangular Waveguides", *29th European Microwave Conference Dig.,* pp. 199-202, Munich, Germany, Oct. 5-7, 1999.

[17] H. E. King, "Rectangular Waveguide Theoretical CW Average Power Rating", *IRE Trans. Microwave Theory and Techniques*, 1961.

[18] C. J. Hsu, "Shape Factor Equations for Radiant Heat Transfer between Two Arbitrary Sizes of Rectangular Planes", Canadian Journal Chem. Eng., vol. 45, 1967.

[19] R. Siegel, J. R. Howell, *Thermal Radiation Heat Transfer*, McGraw-Hill, Inc., New York, 1972.

[20] B. Sunden, M. Faghri, *Modeling of Engineering Heat Transfer Phenomena*, Volume 2, Computational Mechanics Publications, Billerica, MA, 1999.

[21] E. R. G. Eckert, R. J. Goldstein, *Measurements in Heat Transfer*, 2nd Edition, Hemisphere Publishing Corporation, New York, 1976.

[22] J. R. Welty, *Engineering Heat Transfer*, John Wiley & Sons, Inc., New York, 1974.

[23] L. C. Thomas, *Heat Transfer*, Prentice-Hall, Inc., Florida, 1993.

[24] G. Walker, *Industrial Heat Exchangers*, 2nd Edition, Hemisphere Publishing, New York, 1990.

[25] G. L. Ragan, *Microwave Transmission Circuits*, M. I. T. Rad. Lab. Ser., McGraw-Hill Book Co., Inc., New York, N. Y., vol. 9, p. 55, 1948.

[26] R. F. Speyer, *Thermal Analysis of Materials*, Marcel Dekker, Inc., New York, 1994.

[27] A. J. Chapman, *Heat Transfer,* 4th Edition, MacMillan, New York, 1984.

[28] Y. Jaluria, K. E. Torrance, *Computational Heat Transfer*, Hemisphere Publishing Corporation, New York, 1986.

[29] A.F. Mills, *Heat Transfer*, Richard D. Irwin, Inc., Boston, 1992.

[30] J. Shackelford, W. Alexander, *The CRC Materials Science and Engineering Handbook*, CRC Press, Inc., Florida, 2000.

[31] M. Shashkov, *Conservative Finite -Difference Methods on General Grids*, CRC Press, Inc. New York, 1996.

[32] P. Bhartia, I. J. Bahl, *Millimeter Wave Engineering and Applications*, John Wiley & Sons, Inc., 1984.

[33] E. Angel, *Computer Graphics*, Addison-Wesley Publishing Company, Inc., New York, 1990.

[34] T. L. Kunii, *Computer Graphics*, Springer-Verlag, Tokyo, 1985.

[35] A.P. S. Wang, *C++ with Object – Oriented Programming*, PWS Publishing Company, Boston, 1994.

[36] N. M. Josuttis, *The C++ Standard Library*, Addison Wesley Longman, Inc., Reading, MA, 1999.

[37] W. H. Press, B. P. Flannery, S. A. Teukolsky, W. T. Vetterling, *Numerical Recipes*, Cambridge University Press, New York, 1986.

[38] D. Harris, *Computer Graphics and Applications*, Chapman and Hall, Cambridge University Press, London, 1984.

VITA

Surname: Liu Given Name: Wei

Place of Birth: Jiujiang, China Date of Birth: June 16, 1976

Educational Institutions Attended:

University of Victoria	1998 to 2001
University of Science and Technology of China	1993 to 1998

Degree Awarded:

B. Eng.	University of Science and Technology of China	1998

Honors and Awards:

University of Victoria President Petch Research Scholarship	10/1999
Martlet Chapter IODE Graduate Scholarship	10/1999
University of Victoria Fellowship	09/1998 to 08/2000
ASI Graduate Recruitment Scholarship	09/1998
USTC (China) 1998 Excellent Graduation Thesis	07/1998
USTC (China) P&G Scholarship (Industry Sponsor)	09/1997 to 07/1998
USTC (China) Di'ao Scholarship (Industry Sponsor)	09/1996 to 07/1997
USTC (China) Excellent Student Scholarship	09/1994 to 07/1995

Publications:

W. Liu and W. J. R. Hoefer, "Theoretical and Numerical Time Domain Study of Apparently Superluminal Signals in Waveguides", *Fourth International Workshop on Computational Electromagnetics in the Time-Domain, TLM, FDTD and Related Techniques*, Nottingham, UK, September 17-19, 2001.

W. Liu, P. P. M. So and W. J. R. Hoefer, "Coupled TLM-Thermal Analysis in the Time Domain", *IEEE MTT-S International Microwave Symposium Digest*, Phoenix, Arizona, May 21–24, 2001.

W. Liu and W. J. R. Hoefer, "A Study of Apparently Superluminal Signal Transmission in Rectangular Waveguides Below Cutoff", *URSI International Symposium Digest on Electromagnetic Theory*, Victoria, B.C., May 13-17, 2001.

Publications Continued:

W. Liu, P. P. M. So and W. J. R. Hoefer, "Hybrid Modeling of Thermal Behavior of Metallic and Dielectric Objects Exposed to Waveguide Cavity Fields", *The 17th Annual Review of Progress in Applied Computational Electromagnetics*, Monterey, California, March 19-23, 2001.

P. P. M. So, W. Liu, J. W. Park and W. J. R. Hoefer, "Application of Coupled TLM–Thermal Analysis to Embedded Devices", *Fourth International Workshop on Computational Electromagnetics in the Time-Domain, TLM, FDTD and Related Techniques*, Nottingham, UK, September 17-19, 2001.

E. Hu, P. P. M So, M. Fujii, W. Liu and W. J. R. Hoefer, "Performance Comparisons of TLM, FDTD and Haar Wavelet MRTD Algorithms for Electromagnetic Simulations", *Conference Proceedings of Symposium on Antenna Technology and Applied Electromagnetics*, Winnipeg, Manitoba, July 30 - August 2, 2000.

E. Hu, M. Fujii, P. P. M So, W. Liu, J. W. Park and W. J. R. Hoefer, "High Performance Computation for Time Domain Electromagnetic Simulations", *The 14th Annual International Symposium on High Performance Computing Systems and Applications*, Victoria, B.C., June 13-16, 2000.

P. P. M. So, E. Q. Hu, M. Fujii, W. Liu and W. J. R. Hoefer, "Visualization of Near-Field and Far-Field in the Time Domain", *IEEE MTT-S International Microwave Symposium Digest*, Boston, Massachusetts, June 11–16, 2000.

E. Hu, P. P. M. So, M. Fujii, W. Liu and W. J. R. Hoefer, "The Implementation of A High Level (1st-order) Haar Wavelet MRTD Scheme", *The 16th Annual Review of Progress in Applied Computational Electromagnetics*, Monterey, California, March 20-24, 2000.

M. Fujii, P. P. M. So, E. Hu, W. Liu and W. J. R. Hoefer, "A 2D TLM and Haar MRTD Real-Time Hybrid Connection Technique", *The 16th Annual Review of Progress in Applied Computational Electromagnetics*, Monterey, California, March 20-24, 2000.

M. Fujii, P. P. M. So, E. Hu, W. Liu and W. J. R. Hoefer, "Hybrid Connection between TLM and Haar MRTD Algorithms", *Proceedings of TLM Workshop*, Antipolice, Nice-sophia, France, Oct. 1999.

PARTIAL COPYRIGHT LICENSE

I hereby grant the right to lend my thesis to users of the University of Victoria Library, and to make single copies only for such users or in response to a request from the library of any other university, or similar institution, on its behalf or for one of its users. I further agree that permission for extensive copying of this thesis for scholarly purpose may be granted by me or a member of the University designated by me. It is understood that copying or publication of this thesis for financial gain shall not be allowed without my written permission.

Title of Thesis:

Time Domain Modeling of Hybrid Electromagnetic and Thermal Processes

Author 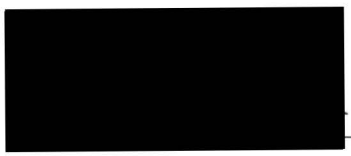

Wei Liu

Mar. 15, 2001